The Astrophysical Journal Supplement Series, 252:3 (19pp), 2021 January https://doi.org/10.3847/1538-4365/abc16e

591 High-velocity Stars in the Galactic Halo Selected from LAMOST DR7 and Gaia DR2

Yin-Bi Li (李荫碧)[1], A-Li Luo (罗阿理)[1,2], You-Jun Lu (陆由俊)[1,2], Xue-Sen Zhang (张学森)[3], Jiao Li (李蛟)[1,4], Rui Wang (王瑞)[1], Fang Zuo (左芳)[1,2], Maosheng Xiang (向茂盛)[5], Yuan-Sen Ting (丁源森)[6,7,8,9], Tommaso Marchetti[10], Shuo Li (李硕)[1,2], You-Fen Wang (王有芬)[1], Shuo Zhang (张硕)[11,12], Kohei Hattori[13,14], Yong-Heng Zhao (赵永恒)[1,2], Hua-Wei Zhang (张华伟)[11,12], and Gang Zhao (赵刚)[1,2]

[1] CAS Key Laboratory of Optical Astronomy, National Astronomical Observatories, Chinese Academy of Sciences, Beijing 100101, People's Republic of China
lal@bao.ac.cn, luyj@bao.ac.cn, gzhao@bao.ac.cn
[2] School of Astronomy and Space Science, University of Chinese Academy of Sciences, Beijing 100049, People's Republic of China
[3] ExtantFuture (Beijing) Technology Co., Ltd, Beijing 100102, People' Republic Of China
[4] Yunnan Observatories, Chinese Academy of Sciences, Kunming 650011, People's Republic of China
[5] Max-Planck Institute for Astronomy, Konigstuhl 17, D-69117 Heidelberg, Germany
[6] Institute for Advanced Study, Princeton, NJ 08540, USA
[7] Department of Astrophysical Sciences, Princeton University, Princeton, NJ 08540, USA
[8] Observatories of the Carnegie Institution of Washington, 813 Santa Barbara St., Pasadena, CA 91101, USA
[9] Research School of Astronomy & Astrophysics, Australian National University, Cotter Rd., Weston, ACT 2611, Australia
[10] European Southern Observatory, Karl Schwarzschild-Strasse 2, 85748 Garching bei Munchen, Germany
[11] Department of Astronomy, School of Physics, Peking University, Beijing 100871, People's Republic of China
[12] Kavli Institute for Astronomy and Astrophysics, Peking University, Beijing 100871, People's Republic of China
[13] National Astronomical Observatory of Japan, 2-21-1 Osawa, Mitaka, Tokyo 181-0015, Japan
[14] Institute of Statistical Mathematics, 10-3 Midoricho, Tachikawa, Tokyo 190-0014, Japan
Received 2020 July 21; revised 2020 October 9; accepted 2020 October 10; published 2020 December 17

Abstract

In this paper, we report 591 high-velocity star candidates (HiVelSCs) selected from over 10 million spectra of Data Release 7 (DR7) of the Large Sky Area Multi-object Fiber Spectroscopic Telescope and the second Gaia data release, with three-dimensional velocities in the Galactic rest frame larger than 445 km s^{-1}. We show that at least 43 HiVelSCs are unbound to the Galaxy with escape probabilities larger than 50%, and this number decreases to eight if the possible parallax zero-point error is corrected. Most of these HiVelSCs are metal-poor and slightly α-enhanced inner halo stars. Only 14% of them have [Fe/H] > -1, which may be the metal-rich "in situ" stars in the halo formed in the initial collapse of the Milky Way or metal-rich stars formed in the disk or bulge but kinematically heated. The low ratio of 14% implies that the bulk of the stellar halo was formed from the accretion and tidal disruption of satellite galaxies. In addition, HiVelSCs on retrograde orbits have slightly lower metallicities on average compared with those on prograde orbits; meanwhile, metal-poor HiVelSCs with [Fe/H] < -1 have an even faster mean retrograde velocity compared with metal-rich HiVelSCs. To investigate the origins of HiVelSCs, we perform orbit integrations and divide them into four types, i.e., hypervelocity stars, hyper-runaway stars, runaway stars and fast halo stars. A catalog for these 591 HiVelSCs, including radial velocities, atmospheric parameters, Gaia astrometric parameters, spatial positions, and velocities, etc., is available in the China-VO PaperData Repository at doi:10.12149/101038.

Unified Astronomy Thesaurus concepts: High-velocity stars (736)

1. Introduction

High-velocity stars move fast, and they mark the presence of extreme dynamical and astrophysical processes, especially when a star approaches or even exceeds the escape velocity of the Galaxy at its position (Hills 1988; Yu & Tremaine 2003; Bromley et al. 2006; Abadi et al. 2009; O'Leary & Loeb 2008; Capuzzo-Dolcetta & Fragione 2015; Marchetti et al. 2019). These stars provide insight into a wide range of Galactic science, on scales from a few parsecs near the central massive black hole (MBH) to the distant Galactic halo, including the dynamical mechanisms that produce their extreme velocities (Zhang et al. 2010; Hawkins et al. 2015), and their distributions in space and velocity, which can reveal the existence of a binary MBH (Zhang et al. 2010; Brown 2015; Fragione & Gualandris 2018; Fragione et al. 2018). They are powerful tracers used to probe the mass distribution of the Galaxy because they travel large distances across it (Gnedin et al. 2005; Kenyon et al. 2008), and their trajectories can also be used to probe the shape of the Galaxy's dark matter halo (Yu & Madau 2007; Kenyon et al. 2008).

In general, there are four subclasses of high-velocity stars including "hypervelocity star" (HVS), "runaway star" (RS), "hyper-runaway star" (HRS), and "fast halo star" (OUT), and they have different origins. The fastest stars in our Galaxy are HVSs, and their proposed ejection mechanisms include: the tidal breakup of binary stars by a single MBH in the Galactic center (GC; Hills 1988; Yu & Tremaine 2003; Bromley et al. 2006), single-star encounters with a binary MBH (Yu & Tremaine 2003; Sesana et al. 2006, 2007), single-star encounters with a cluster of stellar mass black holes around the MBH (O'Leary & Loeb 2008), and the interaction between a globular cluster with a single or binary MBH in the GC (Capuzzo-Dolcetta & Fragione 2015; Fragione & Capuzzo-Dolcetta 2016). RSs are the second subclass of high-velocity stars, and they are thought to have formed in the disk and were then ejected into the halo. RSs can be produced through two main formation mechanisms: supernova explosions in stellar binary systems (e.g., Blaauw 1961; Gvaramadze et al. 2009; Wang & Han 2009; Wang et al. 2013), and dynamical interactions due to multibody encounters in dense stellar

systems (e.g., Bromley et al. 2009; Gvaramadze et al. 2009). If an RS has such an extremely high velocity that it can escape from the Galaxy, it belongs to the third subclass of high velocity stars, i.e., to the HRSs (Perets & Šubr 2012; Brown 2015; Li et al. 2018). The last subclass of high-velocity stars is the fast halo stars, and they can be produced by the tidal interactions of dwarf galaxies near the GC (Abadi et al. 2009), or from other galaxies in the Local Group (Sherwin et al. 2008; Teyssier et al. 2009), for example from the center of the Large Magellanic Cloud (LMC; Boubert & Evans 2016; Boubert et al. 2017).

The first hypervelocity star (HVS1) was serendipitously discovered by Brown et al. (2005), and it is a late-B-type star with a heliocentric distance ∼71 kpc and radial velocity (RV) ∼ 853 km s^{-1}. Since then, the number of high-velocity star candidates (HiVelSCs) has ballooned, and there are nearly 500 candidates in the literature before Gaia Data Release 2 (DR2) (Edelmann et al. 2005; Hirsch et al. 2005; Brown et al. 2006, 2009, 2012, 2014; Heber et al. 2008; Kollmeier et al. 2009; Tillich et al. 2009; Li et al. 2012, 2015; Zheng et al. 2014; Zhong et al. 2014; Favia et al. 2015; Huang et al. 2017; Vennes et al. 2017). Most of these stars are late-type high-proper-motion stars, and about two dozen of them are faint and blue stars in the halo that were classified as HVSs based only on their extreme RVs.

After Gaia DR2, new high-velocity stars were searched for with more precise astrometric parameters (Bromley et al. 2018; Hattori et al. 2018; Irrgang et al. 2018a, 2019; Li et al. 2018; Shen et al. 2018; de la Fuente Marcos & de la Fuente Marcos 2019; Raddi et al. 2019; Caffau et al. 2020; Koposov et al. 2020; Li et al. 2020). For example, Li et al. (2018) found a new late-B-type HRS from the Large Sky Area Multi-object Fiber Spectroscopic Telescope (LAMOST) with Gaia DR2 proper motions, and it has a total Galactocentric velocity of ∼586 km s^{-1}. Hattori et al. (2018) reported the discovery of 30 old metal-poor stars with extreme velocities (>480 km s^{-1}) in Gaia DR2; up to three of these stars were purported to be ejected from the LMC, and one or two stars originated from the GC. Marchetti et al. (2019) found 20 stars that have probabilities >80% of being unbound from the Galaxy, seven of them are HRSs, and another 13 stars may not have their origins in the Galaxy. Shen et al. (2018) found three hyper-runaway white dwarfs in Gaia DR2, which have total Galactocentric velocities between 1000 and 3000 km s^{-1}. Except for these newly discovered high-velocity stars, previously known HVSs were also revisited to further investigate their possible origins by tracing their orbits back in time with new Gaia astrometric parameters (Boubert et al. 2018; Brown et al. 2018; Irrgang et al. 2018a; Erkal et al. 2019; Kreuzer et al. 2020). For example, Erkal et al. (2019) reanalyzed 26 previously known HVSs and found that the third HVS (HE 0437-5439 or HVS3) is likely to be coming almost from the center of the LMC, and Boubert et al. (2018) found that almost all previously known late-type high-velocity stars are likely bound to the Milky Way and only one late-type object (LAMOST J115209.12+120258.0) is unbound from the Galaxy (Li et al. 2018).

Du et al. (2018a, 2018b) successively searched for HiVelSCs from the early data version of LAMOST and Gaia, and the second work only focuses on spectra also having Gaia RVs (LAMOST provides RV data for all stellar spectra, but Gaia provides these data only for a small fraction of spectral types), which is a sample smaller than that corresponding to the LAMOST data they used. As mentioned in Boubert et al. (2019) and Li et al. (2020), RVs of Gaia DR2 could be spurious if light contamination exists from a nearby bright star. To avoid this problem, we only use LAMOST RVs to estimate spatial velocities, and search for HiVelSCs from the latest data version of LAMOST (DR7) and Gaia (DR2). Besides, a different target selection method and distance and velocity estimation methods are adopted in this work, which leads to a different search result for HiVelSCs.

Up to now, only a few studies have used both the chemical and kinematic information of high-velocity stars to determine where they were produced and how they achieved such high velocities (Geier et al. 2015; Hawkins et al. 2015; Du et al. 2018a, 2018b; Irrgang et al. 2018b; Marchetti et al. 2019). In this paper, we use the chemistry and kinematics simultaneously to investigate the possible origins and stellar populations for high-velocity stars, and find a few possible "in situ" halo stars. We also analyze the kinematic properties for metal-poor and metal-rich stars, respectively, and the chemical properties for prograde and retrograde stars.

The paper is organized as follows. In Section 2, we describe the method that we used to search for HiVelSCs. In Section 3, we analyze the spatial position and velocity distributions of our HiVelSCs, their stellar population, and their chemical and kinematic properties. In Section 4, we calculate orbit parameters for HiVelSCs, and investigate their possible origins. In Section 5, we discuss the impact of a −0.029 mas global parallax zero-point, and the results that adopt more conservative criteria to select HiVelSCs. Finally, the conclusions are presented in Section 6.

2. Data

2.1. LAMOST and Gaia

LAMOST is a 4 m quasi-meridian reflective Schmidt telescope, which is equipped with 4000 fibers and can observe up to 4000 targets per exposure simultaneously (Wang et al. 1996; Su & Cui 2004; Zhao et al. 2006, 2012; Cui et al. 2012; Luo et al. 2012). From 2011–2018, LAMOST completed its first-stage low-resolution spectroscopic survey ($R \sim 1800$), and obtained more than 9 million spectra.[15] Since October 2018, LAMOST started the second-stage survey (LAMOST II), which contains both low- and medium-resolution spectroscopic surveys. LAMOST II uses about half of the available nights to continue the previous low-resolution survey, and the other half (bright/gray nights) for the medium-resolution survey (Liu et al. 2020). In 2020 March, DR7 of the low-resolution spectroscopic survey provided 10,608,416 low-resolution spectra,[16] and these spectra cover the wavelength range of 3690–9100 Å with a resolution of $R \sim 1800$ at 4750 Å (blue) and 7350 Å (red), respectively. The LAMOST Stellar Parameter Pipeline (LASP) estimates atmospheric parameters and RV, and it has an accuracy of about 150 K, 0.25 dex, 0.15 dex, and 5.0 km s^{-1} for the effective temperature ($T_{\rm eff}$), surface gravity ($\log g$), metallicity ([Fe/H]), and RV, respectively (Luo et al. 2015; Xiang et al. 2015), for spectra of signal-to-noise ratios (S/Ns) higher than 10.

Gaia is a space-based mission in the science program of the European Space Agency launched in 2013, and its main aim is

[15] http://dr5.lamost.org/
[16] http://dr7.lamost.org/

to measure the astrometric parameters of stars, and to understand the formation, structure, and evolution of the Milky Way (see the review by Bland-Hawthorn & Gerhard 2016). On 2018 April 25, Gaia delivered its second date release (DR2; Gaia Collaboration et al. 2016, 2018a), and it provides precise positions (α, δ), proper motions (μ_{α^*}, μ_δ), parallaxes (ϖ), and photometries for over 1.3 billion stars brighter than magnitude 21 (Gaia Collaboration et al. 2018a, 2018b). The median uncertainty in parallax and position (at the reference epoch J2015.5) is about 0.04 mas at $G < 14$ mag, 0.1 mas at $G = 17$ mag, and 0.7 mas at $G = 20$ mag, and the corresponding uncertainties of the proper motion components are 0.05, 0.2, and 1.2 mas yr^{-1}, respectively (Lindegren et al. 2018).

2.2. Distance and Total Velocity Determination

Using the five astrometric parameters in the Gaia DR2 catalog and RV in the LAMOST catalog, Galactocentric distance ($r_{\rm GC}$) and total velocity ($V_{\rm GC}$) are computed based on the following assumptions: (1) the distance between the Sun and the GC is $d_\odot = 8.2$ kpc, and the Sun has an offset above the stellar disk of $z_\odot = 25$ pc (Bland-Hawthorn & Gerhard 2016); (2) the motion of the local standard of rest (LSR) is 238 km s^{-1}, and the velocity of the Sun with respect to the LSR is $[U_\odot, V_\odot, W_\odot] = [14.0, 12.24, 7.25]$ km s^{-1} (Schönrich et al. 2010; Schönrich 2012; Bland-Hawthorn & Gerhard 2016); (3) the distribution of equator coordinates, parallax, and proper motions is a multivariate Gaussian with a mean vector $m = [\alpha, \delta, \varpi, \mu_{\alpha*}, \mu_\delta]$, and a covariance matrix:

$$\Sigma = \begin{pmatrix} \sigma_\alpha^2 & \sigma_\alpha\sigma_\delta\rho(\alpha,\delta) & \sigma_\alpha\sigma_\varpi\rho(\alpha,\varpi) & \sigma_\alpha\sigma_{\mu_{\alpha^*}}\rho(\alpha,\mu_{\alpha^*}) & \sigma_\alpha\sigma_{\mu_\delta}\rho(\alpha,\mu_\delta) \\ \sigma_\delta\sigma_\alpha\rho(\delta,\alpha) & \sigma_\delta^2 & \sigma_\delta\sigma_\varpi\rho(\delta,\varpi) & \sigma_\delta\sigma_{\mu_{\alpha^*}}\rho(\delta,\mu_{\alpha^*}) & \sigma_\delta\sigma_{\mu_\delta}\rho(\delta,\mu_\delta) \\ \sigma_\varpi\sigma_\alpha\rho(\varpi,\alpha) & \sigma_\varpi\sigma_\delta\rho(\varpi,\delta) & \sigma_\varpi^2 & \sigma_\varpi\sigma_{\mu_{\alpha^*}}\rho(\varpi,\mu_{\alpha^*}) & \sigma_\varpi\sigma_{\mu_\delta}\rho(\varpi,\mu_\delta) \\ \sigma_{\mu_{\alpha^*}}\sigma_\alpha\rho(\mu_{\alpha^*},\alpha) & \sigma_{\mu_{\alpha^*}}\sigma_\delta\rho(\mu_{\alpha^*},\delta) & \sigma_{\mu_{\alpha^*}}\sigma_\varpi\rho(\mu_{\alpha^*},\varpi) & \sigma_{\mu_{\alpha^*}}^2 & \sigma_{\mu_{\alpha^*}}\sigma_{\mu_\delta}\rho(\mu_{\alpha^*},\mu_\delta) \\ \sigma_{\mu_\delta}\sigma_\alpha\rho(\mu_\delta,\alpha) & \sigma_{\mu_\delta}\sigma_\delta\rho(\mu_\delta,\delta) & \sigma_{\mu_\delta}\sigma_\varpi\rho(\mu_\delta,\varpi) & \sigma_{\mu_\delta}\sigma_{\mu_{\alpha^*}}\rho(\mu_\delta,\mu_{\alpha^*}) & \sigma_{\mu_\delta}^2 \end{pmatrix}, \quad (1)$$

where $\rho(i, j)$ is the correlation coefficient between the astrometric parameters i and j, and is provided by the Gaia DR2. LAMOST RV is uncorrelated to the astrometric parameters, thus we assume it follows a Gaussian distribution, which is centered on RV and with a standard deviation of $\sigma_{\rm RV}$ (uncertainty on RV; Marchetti et al. 2019).

To estimate $r_{\rm GC}$ and $V_{\rm GC}$, the Monte Carlo (MC) method is applied. For each star, 1000 MC samplings on its five astrometric parameters and RV are performed, and 1000 $r_{\rm GC}$ and $V_{\rm GC}$ can be obtained according to above assumptions. The Galactic Cartesian coordinate system adopted here is centered on the GC. The x-axis points from the Sun to the GC, the y-axis points in the direction of Galactic rotation, and the z-axis points toward the Northern Galactic Pole (Johnson & Soderblom 1987; Li et al. 2012). We use the median (50th percentile) and the 16th and 84th percentiles as the computed parameters and their lower and upper uncertainties, respectively (de la Fuente Marcos & de la Fuente Marcos 2019; Marchetti et al. 2019).

Lindegren et al. (2018) pointed that the Gaia DR2 parallax has a global zero-point of −0.029 mas, which indicates that the parallaxes are underestimated and hence the distances are overestimated if the usual inverse relationship is adopted. However, both Lindegren et al. (2018) and Arenou et al. (2018) explicitly discouraged a global zero-point correction, particularly in cases where the sample is not well distributed over the entire sky. In addition, Arenou et al. (2018) showed that the parallax offset is partly dependent on the scanning pattern of Gaia, which makes it a function of the coordinates. Taking these into account, we do not correct the parallax zero-point here, and discuss the changes on distances and velocities if the zero-point correction were to be considered in Section 5.

2.3. Sample Selection

Using the parallax in the Gaia DR2 catalog, the heliocentric distance can be determined just by inverting the parallax: $d = 1/\varpi$. However, Bailer-Jones (2015) discussed that this naive approach fails for nonpositive parallaxes, and can induce strong biases for fractional parallax errors, i.e., $f_\varpi = \sigma_\varpi/\varpi$, larger than about 20%. In this paper, we only focus on stars with positive parallaxes ($\varpi > 0$) and smaller fractional parallax errors of $f_\varpi \leqslant 0.2$ (the "low-f" samples).

Using the TOPCAT,[17] a cross match of LAMOST DR7 with Gaia DR2 was performed with a radius of 5″, and the output was a catalog (LAMOST-Gaia hereafter) consisting of over 10 million entries, which includes both LAMOST and Gaia parameters, for example, RV, five Gaia astrometric parameters, magnitudes, and correlation coefficients. In the LAMOST-Gaia catalog, there are over 8.48 million "low-f" entries, and their $r_{\rm GC}$ and $V_{\rm GC}$ are estimated as described in Section 2.2. Seven Galactic potential models (Paczynski 1990; Gnedin et al. 2005; Xue et al. 2008; Koposov et al. 2010; Kenyon et al. 2014; Bovy 2015; Watkins et al. 2019, hereinafter Paczynski+1990, Gnedin+2005, Xue+2008, Koposov+2010, Kenyon+2014, MWPotential2014, and Watkins+2019) are adopted here to estimate the escape velocities, and 31,440 samples are picked out with the condition of either escaping from our Galaxy under at least one potential model or bound but at least with total velocities of $V_{\rm GC} \geqslant 450$ km s^{-1} as used in Marchetti et al. (2019) to select HiVelSCs. We then check the spectral qualities and only retain spectra with the highest S/Ns for stars with multiple observations, and 1761 stars are left. In previous steps, we use the RV provided by the LAMOST 1D pipeline ($\rm RV_{1D}$) to calculate the total velocity, and did not consider the reliability of RV. To select candidates with reliable RVs, we inspect the spectra for 1761 stars to check whether the spectral line shift is consistent with $\rm RV_{1D}$, and 591 HiVelSCs with reliable $\rm RV_{1D}$s are finally selected.

[17] http://www.star.bris.ac.uk/~mbt/topcat/

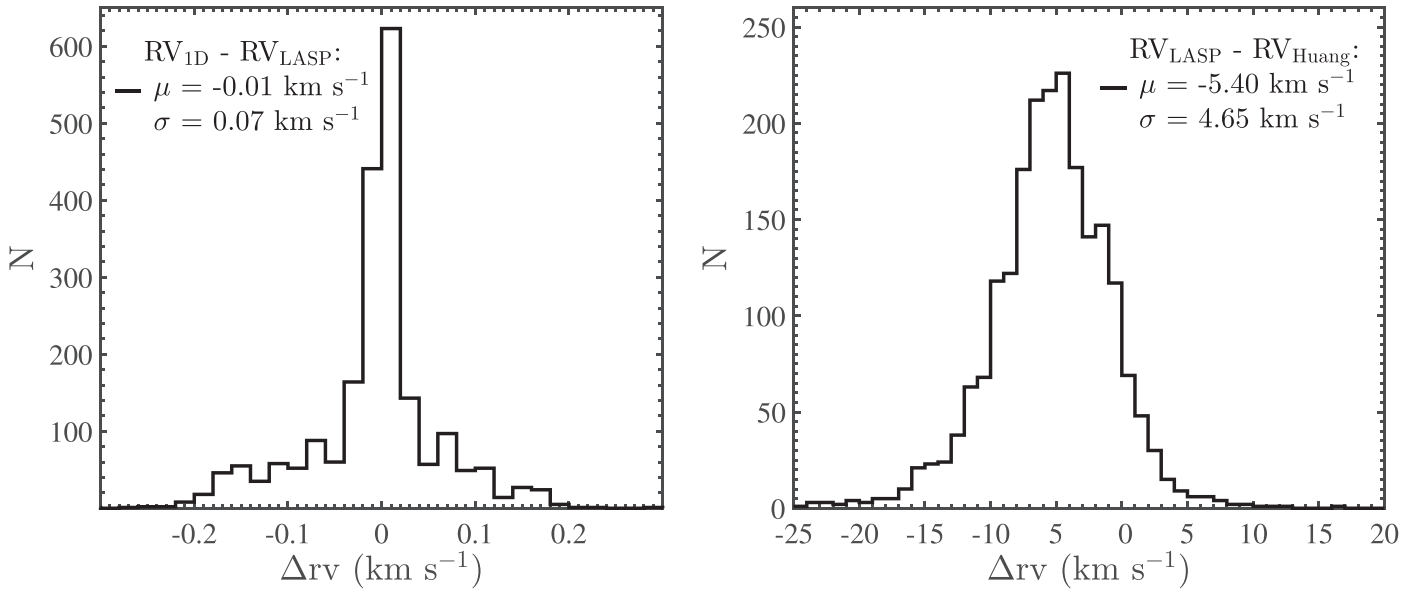

Figure 1. A cross match between a catalog of radial velocity standard stars provided by Huang et al. (2018) and LAMOST DR7 catalog were performed, and obtained 2125 common stars. These stars were used to investigate the consistency of radial velocities given by the LAMOST 1D pipeline (RV_{1D}) and by the LAMOST Stellar Parameter Pipeline (RV_{LASP}) and the radial velocity zero-point, and about 93% of their spectra have S/Ns larger than 40. Left panel: the difference between RV_{1D} and RV_{LASP}. Right panel: the difference between RV_{1D} and radial velocities in the radial velocity standard star catalog (RV_{Huang}). A mean difference of $\mu = -0.01$ km s^{-1} indicates that the RV_{1D} is consistent with RV_{LASP}, which is used to recalculate Galactocentric total velocity (V_{GC}) for 592 HiVelSCs, and RV_{LASP} is shown in our high-velocity star candidate catalog instead of RV_{1D}. A mean difference $\mu = -5.40$ km s^{-1} implies the zero-point of RV_{LASP} is -5.40 km s^{-1}, which is used to perform the zero-point correction for 592 HiVelSCs.

In the public stellar parameter catalog of LAMOST, RV, atmospheric parameters, and their errors were determined by the LAMOST Stellar Parameter Pipeline (LASP) using the method mentioned in A.-L. Luo et al. (2020, in preparation). This work not only considers the calculation error of the LASP but also includes the errors introduced by observation and data processing. Thus, the calculation of the LASP RV (RV_{LASP}) error takes into account more factors, which may make the outcome closer to the true RV errors. To be consistent with the public LAMOST parameter catalog and use more reasonable RV uncertainties, we adopt the RV_{LASP} as our final RVs for 591 HiVelSCs.

We then correct the zero-point of RV_{LASP} for all HiVelSCs using a catalog of 18,080 radial velocity standard stars (Huang et al. 2018) selected from the APO Galactic Evolution Experiment data, and it is also used to investigate the consistency of RV_{1D} and RV_{LASP}. We cross-match the catalog of radial velocity standard stars with LAMOST DR7, and obtain 2125 common stars. For these stars, the distribution of difference between RV_{1D} and RV_{LASP} is shown in the left panel of Figure 1, and we can see that these stars yield a mean difference of $\mu = -0.01$ km s^{-1} and a standard deviation of $\sigma = 0.07$ km s^{-1}, which represents that RV_{1D} is well consistent with RV_{LASP}. The distribution of difference between RV_{LASP} and RV in the catalog of radial velocity standard stars (RV_{Huang}) for these common stars is shown in the right panel of Figure 1, and we see that a mean difference of $\mu = -5.40$ km s^{-1} and a standard deviation of $\sigma = 4.65$ km s^{-1} exist, which means that the zero-point of RV_{LASP} is -5.4 km s^{-1}. After a zero-point correction of -5.4 km s^{-1} for RV_{LASP}, we recalculate the spatial velocities for 591 HiVelSCs, and find that the recalculated median V_{GC} are all larger than 445 km s^{-1}.

2.4. High-velocity Star Candidates

After the above steps in Section 2.3, 591 HiVelSCs are finally selected from the LAMOST-Gaia catalog, and only 14 of them were reported in the current version of the Open Fast Stars Catalog[18] (OFSC; Boubert et al. 2018), which contains a collection of 558 HiVelSCs in the literature. Du et al. (2018a, 2018b) reported 16 (Du1) and 24 (Du2) high-velocity stars, respectively, which were both found from LAMOST and Gaia with different data, and nine of them in total were also reported in the OFSC. We cross-match 591 HiVelSCs with Du1 and Du2 in a radius of 3″, respectively, and find that 12 out of our 591 HiVelSCs were already reported in Du2.

We construct a catalog including 93 columns to list various parameters for these 591 HiVelSCs, i.e., "LAMOSTDR7-GAIADR2-HiVelSC," and Table A4 explains each column of this table in detail. The 4th to 21st columns of Table A4 are listed in Table 1 for the 20 fastest HiVelSCs, such as equatorial coordinate, Gaia parallax, and magnitude, and the 26th to 61st columns are listed in Table 2 also for the 20 fastest HiVelSCs.

The spatial distribution of the 591 HiVelSCs in Galactic coordinates is plotted in Figure 2, and the black solid dots are 558 stars in the OFSC. The red and blue solid dots represent 591 HiVelSCs, and the blue solid dots are 92 conservative HiVelSCs, which are introduced in detail in Section 5.2. The dashed magenta rectangle shows the region of the LAMOST Galactic anticentre survey (Yuan et al. 2015), which collects over 3.6 million spectra accounting for at least 34% of all DR7-released spectra, but only about 10 HiVelSCs are found in this region, which accounts for about 1.7% of all HiVelSCs.

The G magnitude distribution of Gaia DR2 is shown in Figure 3, and the black histogram is the distribution for 558

[18] https://faststars.space/

Table 1
Basic Parameters for the 20 Fastest High-velocity Star Candidates (HiVelSCs)

ID	R.A. (deg)	Decl. (deg)	S/N_r[a]	Class[b]	RV_{LASP}[c] (km s^{-1})	pmra[d] (mas yr^{-1})	pmdec[d] (mas yr^{-1})	parallax[e] (mas)	G[f] (mag)	G_{BP}[f] (mag)	G_{RP}[f] (mag)	astrometric_flag[g]
Hivel1	240.3374980	41.16681800	158	G7	−179 ± 5	−25.759 ± 0.025	−9.745 ± 0.040	0.118 ± 0.016	13.01	13.00	15.21	0
Hivel2	193.4372560	55.05813200	29	F9	−225 ± 14	−23.742 ± 0.042	−39.545 ± 0.041	0.197 ± 0.029	15.63	13.19	13.89	1
Hivel3	102.4840100	46.83601200	33	K5	−75 ± 6	142.070 ± 0.091	−285.151 ± 0.084	1.345 ± 0.092	14.39	16.20	16.92	0
Hivel4	171.7747380	42.40792700	135	A1V	109 ± 4	−39.672 ± 0.054	−26.943 ± 0.076	0.214 ± 0.042	14.62	12.69	13.25	0
Hivel5	212.4778050	33.71299000	34	F6	−252 ± 10	−17.612 ± 0.019	−16.573 ± 0.034	0.105 ± 0.019	13.09	12.51	13.51	1
Hivel6	240.5153620	9.52531900	153	G2	172 ± 8	−3.737 ± 0.035	−24.323 ± 0.023	0.126 ± 0.024	13.63	12.35	12.54	1
Hivel7	214.9762830	37.66936600	31	F0	−245 ± 15	−42.914 ± 0.038	−17.258 ± 0.050	0.222 ± 0.035	15.83	19.25	19.17	1
Hivel8	194.7713607	−2.54662930	127	G7	92 ± 5	26.920 ± 0.140	−134.331 ± 0.068	0.723 ± 0.063	13.61	13.07	14.00	0
Hivel9	231.8486900	36.03446500	174	G5	−89 ± 4	−15.238 ± 0.027	−14.224 ± 0.041	0.103 ± 0.020	11.19	10.37	11.98	0
Hivel10	329.7058060	1.35603100	24	F7	−52 ± 12	−21.883 ± 0.068	−30.680 ± 0.056	0.213 ± 0.036	14.03	12.97	13.95	0
Hivel11	190.6504160	52.56223400	72	G6	99 ± 6	−12.198 ± 0.022	−13.476 ± 0.022	0.092 ± 0.015	13.42	15.90	18.79	1
Hivel12	187.4196460	24.50598100	153	G3	241 ± 6	−15.178 ± 0.035	−15.656 ± 0.026	0.111 ± 0.022	13.37	12.75	13.84	1
Hivel13	256.3047540	19.94524300	65	G3	−146 ± 7	−8.992 ± 0.021	−26.154 ± 0.024	0.146 ± 0.017	13.91	15.39	17.83	1
Hivel14	288.3732000	42.08276000	84	G7	−316 ± 10	−4.459 ± 0.031	12.781 ± 0.031	0.092 ± 0.017	14.39	16.17	16.80	0
Hivel15	250.9465099	43.60750040	59	F5	−70 ± 13	−16.454 ± 0.070	−36.536 ± 0.106	0.231 ± 0.042	16.03	15.51	18.34	1
Hivel16	216.9762060	29.84803200	115	F0	−40 ± 9	−10.328 ± 0.034	−28.546 ± 0.037	0.159 ± 0.021	13.38	12.96	13.64	1
Hivel17	244.1838800	17.86343200	57	F0	23 ± 16	−49.937 ± 0.052	−19.192 ± 0.049	0.291 ± 0.049	15.54	12.51	13.81	1
Hivel18	258.1346050	40.47350100	90	G3	−218 ± 11	−20.574 ± 0.035	4.683 ± 0.040	0.123 ± 0.021	12.68	14.89	18.18	1
Hivel19	182.5150380	0.98761100	91	G7	223 ± 7	−22.117 ± 0.055	−30.106 ± 0.036	0.195 ± 0.033	13.08	13.61	14.68	1
Hivel20	207.1676590	52.84460600	57	F2	−103 ± 15	−24.004 ± 0.036	−24.524 ± 0.034	0.179 ± 0.025	15.23	12.36	13.51	1

Notes. The 4th to 21st columns of Table A4 are listed here for the 20 fastest HiVelSCs, and the measurement values and the uncertainties are shown in the same column in this table but separated into two columns in Table A4.

[a] r band S/N from LAMOST.

[b] Spectral type given by the LAMOST 1D pipeline.

[c] RV given by the LASP, which is corrected a radial velocity zero-point of −5.4 km s^{-1} mentioned in the last two paragraphs of Section 2.3.

[d] Proper motions from Gaia.

[e] Parallax from Gaia.

[f] G, G_{BP}, and G_{RP} magnitudes from Gaia.

[g] A flag to show whether a candidate has more conservative astrometric parameters.

Table 2
Spatial Positions and Velocities of the 20 Fastest HiVelSCs

ID	x[a] (kpc)	y[a] (kpc)	z[a] (kpc)	r_{GC}[b] (kpc)	V_x[c] (km s^{-1})	V_y[c] (km s^{-1})	V_z[c] (km s^{-1})	V_{GC}[d] (km s^{-1})	e[e]	Z_{max}[f] (kpc)	r_{min}[g] (kpc)	$E-\Phi(\infty)$[h] (kpc^2 Myr^{-2})
Hivel1	$-5.9^{+0.4}_{-0.3}$	$5.1^{+0.8}_{-0.6}$	$6.4^{+1.0}_{-0.8}$	$10.1^{+0.9}_{-0.6}$	-88^{+7}_{-8}	-717^{+104}_{-127}	573^{+108}_{-85}	922^{+168}_{-136}	–	–	$13.7^{+1.9}_{-1.4}$	$0.0033^{+0.0019}_{-0.0013}$
Hivel2	$-9.4^{+0.2}_{-0.2}$	$2.0^{+0.4}_{-0.3}$	$4.5^{+0.8}_{-0.6}$	$10.6^{+0.6}_{-0.4}$	56^{+4}_{-5}	-850^{+132}_{-182}	256^{+85}_{-60}	888^{+197}_{-142}	–	–	$19.1^{+1.8}_{-1.4}$	$0.0030^{+0.0020}_{-0.0012}$
Hivel3	$-8.9^{+0.0}_{-0.0}$	$0.1^{+0.0}_{-0.0}$	$0.3^{+0.0}_{-0.0}$	$8.9^{+0.1}_{-0.0}$	-78^{+12}_{-14}	-866^{+72}_{-80}	110^{+10}_{-8}	876^{+81}_{-73}	–	–	$8.9^{+0.1}_{-0.1}$	$0.0028^{+0.0007}_{-0.0007}$
Hivel4	$-10.0^{+0.3}_{-0.4}$	$0.5^{+0.1}_{-0.1}$	$4.4^{+1.0}_{-0.7}$	$10.9^{+0.8}_{-0.5}$	-613^{+95}_{-137}	-621^{+142}_{-206}	-41^{+24}_{-36}	874^{+247}_{-168}	–	–	$92.9^{+184.4}_{-54.6}$	$0.0026^{+0.0026}_{-0.0012}$
Hivel5	$-6.7^{+0.4}_{-0.2}$	$2.5^{+0.6}_{-0.4}$	$9.0^{+2.0}_{-1.3}$	$11.5^{+1.6}_{-0.9}$	-73^{+7}_{-11}	-857^{+145}_{-237}	66^{+70}_{-43}	862^{+242}_{-147}	–	–	$74.4^{+7.4}_{-6.4}$	$0.0028^{+0.0025}_{-0.0013}$
Hivel6	$-2.6^{+1.2}_{-0.9}$	$2.1^{+0.5}_{-0.4}$	$5.3^{+1.2}_{-0.9}$	$6.3^{+0.8}_{-0.4}$	639^{+113}_{-84}	-454^{+126}_{-168}	-109^{+39}_{-51}	791^{+199}_{-142}	–	–	$195.7^{+541.8}_{-105.9}$	$0.0018^{+0.0018}_{-0.0010}$
Hivel7	$-7.6^{+0.1}_{-0.1}$	$1.5^{+0.3}_{-0.2}$	$4.2^{+0.8}_{-0.6}$	$8.8^{+0.4}_{-0.2}$	-382^{+48}_{-73}	-676^{+112}_{-168}	138^{+73}_{-50}	789^{+194}_{-126}	–	–	$18.2^{+2.2}_{-1.9}$	$0.0020^{+0.0016}_{-0.0010}$
Hivel8	$-7.8^{+0.0}_{-0.0}$	$-0.6^{+0.0}_{-0.1}$	$1.2^{+0.1}_{-0.1}$	$7.9^{+0.0}_{-0.0}$	606^{+51}_{-44}	-334^{+43}_{-51}	-357^{+35}_{-40}	778^{+81}_{-69}	–	–	–	$0.0018^{+0.0007}_{-0.0005}$
Hivel9	$-5.3^{+0.7}_{-0.5}$	$4.6^{+1.1}_{-0.8}$	$8.0^{+2.0}_{-1.3}$	$10.6^{+1.7}_{-1.0}$	172^{+46}_{-31}	-631^{+139}_{-205}	349^{+102}_{-68}	741^{+236}_{-156}	–	–	$20.1^{+4.6}_{-3.4}$	$0.0018^{+0.0019}_{-0.0012}$
Hivel10	$-6.4^{+0.4}_{-0.3}$	$3.1^{+0.7}_{-0.4}$	$-2.9^{+0.4}_{-0.6}$	$7.7^{+0.3}_{-0.1}$	705^{+154}_{-102}	-214^{+61}_{-96}	16^{+8}_{-10}	737^{+174}_{-114}	–	–	$176.9^{+177.2}_{-65.1}$	$0.0015^{+0.0015}_{-0.0008}$
Hivel11	$-10.9^{+0.4}_{-0.6}$	$3.8^{+0.8}_{-0.5}$	$9.8^{+2.0}_{-1.4}$	$15.2^{+2.0}_{-1.2}$	-221^{+28}_{-43}	-583^{+119}_{-181}	371^{+58}_{-37}	727^{+186}_{-123}	–	–	$19.0^{+5.8}_{-4.0}$	$0.0018^{+0.0015}_{-0.0010}$
Hivel12	$-8.6^{+0.1}_{-0.1}$	$-0.8^{+0.1}_{-0.2}$	$9.0^{+2.3}_{-1.4}$	$12.5^{+1.8}_{-1.0}$	-215^{+35}_{-56}	-675^{+144}_{-232}	160^{+15}_{-23}	726^{+230}_{-138}	–	–	$27.7^{+24.4}_{-10.3}$	$0.0016^{+0.0018}_{-0.0010}$
Hivel13	$-3.8^{+0.6}_{-0.4}$	$3.7^{+0.5}_{-0.4}$	$3.6^{+0.5}_{-0.4}$	$6.4^{+0.3}_{-0.1}$	508^{+79}_{-59}	-503^{+69}_{-89}	-87^{+4}_{-4}	718^{+121}_{-87}	–	–	–	$0.0013^{+0.0010}_{-0.0007}$
Hivel14	$-5.2^{+0.7}_{-0.5}$	$10.1^{+2.4}_{-1.6}$	$2.6^{+0.6}_{-0.4}$	$11.6^{+2.0}_{-1.2}$	-593^{+82}_{-120}	-9^{+13}_{-11}	395^{+109}_{-72}	713^{+160}_{-108}	–	–	$10.1^{+2.3}_{-1.3}$	$0.0014^{+0.0015}_{-0.0008}$
Hivel15	$-7.0^{+0.3}_{-0.2}$	$3.0^{+0.7}_{-0.5}$	$2.9^{+0.7}_{-0.4}$	$8.1^{+0.3}_{-0.1}$	614^{+147}_{-94}	-277^{+73}_{-116}	212^{+60}_{-39}	705^{+191}_{-121}	–	–	$16.1^{+2.0}_{-1.4}$	$0.0013^{+0.0014}_{-0.0008}$
Hivel16	$-6.6^{+0.2}_{-0.2}$	$1.6^{+0.2}_{-0.2}$	$5.9^{+0.9}_{-0.7}$	$9.0^{+0.5}_{-0.3}$	397^{+58}_{-46}	-566^{+94}_{-119}	90^{+20}_{-17}	698^{+132}_{-104}	–	–	$37.3^{+8.3}_{-5.8}$	$0.0013^{+0.0012}_{-0.0007}$
Hivel17	$-6.0^{+0.4}_{-0.4}$	$1.4^{+0.3}_{-0.2}$	$2.3^{+0.4}_{-0.4}$	$6.6^{+0.2}_{-0.1}$	-21^{+13}_{-13}	-474^{+117}_{-143}	512^{+95}_{-80}	697^{+165}_{-137}	–	–	$6.8^{+0.1}_{-0.0}$	$0.0010^{+0.0013}_{-0.0007}$
Hivel18	$-5.4^{+0.6}_{-0.4}$	$6.0^{+1.3}_{-0.8}$	$4.7^{+1.0}_{-0.6}$	$9.3^{+1.1}_{-0.6}$	-328^{+38}_{-52}	-304^{+57}_{-76}	538^{+139}_{-92}	697^{+170}_{-110}	–	–	$8.8^{+1.6}_{-1.0}$	$0.0013^{+0.0014}_{-0.0008}$
Hivel19	$-7.7^{+0.1}_{-0.1}$	$-2.4^{+0.3}_{-0.5}$	$4.6^{+1.0}_{-0.7}$	$9.3^{+0.6}_{-0.3}$	-81^{+17}_{-25}	-659^{+118}_{-177}	-207^{+62}_{-87}	696^{+198}_{-131}	–	–	$195.7^{+283.0}_{-186.0}$	$0.0012^{+0.0015}_{-0.0008}$
Hivel20	$-8.8^{+0.1}_{-0.1}$	$2.5^{+0.4}_{-0.3}$	$5.0^{+0.8}_{-0.6}$	$10.5^{+0.6}_{-0.4}$	-31^{+8}_{-9}	-609^{+103}_{-136}	324^{+69}_{-55}	691^{+149}_{-118}	–	–	$13.8^{+1.9}_{-1.2}$	$0.0012^{+0.0012}_{-0.0007}$

Notes. The 26th to 61st columns of Table A4 are listed here for the 20 fastest HiVelSCs, which includes spatial positions and velocities. The median value, the lower uncertainty, and the upper uncertainty of each parameter are shown in the same column in this table but separated into three columns in Table A4 (from the 26th to 61st columns).

[a] Galactocentric spatial position (x, y, z).

[b] Galactocentric distance.

[c] Galactocentric spatial velocity (V_x, V_y, V_z).

[d] Galactocentric total velocity.

[e] Orbit eccentricity, e, "–" represents e is not provided.

[f] Orbital maximum height above the Galactic disk, "–" represents Z_{max} is not provided.

[g] Minimum crossing radius during the orbital trace back.

[h] Energy difference between orbital energy and potential energy at infinity.

[i] For a star, if less than 1% orbits of an MC simulation with N realizations intersect with the Galactic disk, we do not provide r_{min} and its errors, which is represented by the "–." Note that we only provide e and Z_{max} for 246 bound HiVelSCs with $Z_{max} \leqslant 200$ kpc, and "–" represents e and Z_{max} are not provided.

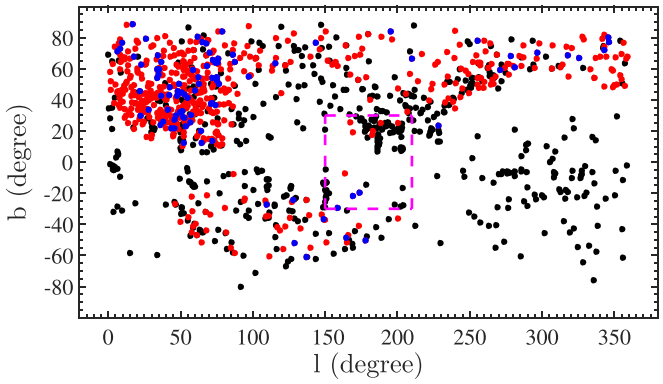

Figure 2. The spatial distribution of 591 HiVelSCs in the Galactic coordinates. The black solid dots are 558 stars in the OFSC, and the red and blue solid dots represent 591 HiVelSCs, 92 of which are conservative HiVelSCs shown by blue solid dots and selected by more conservative criteria described in Section 5.2.

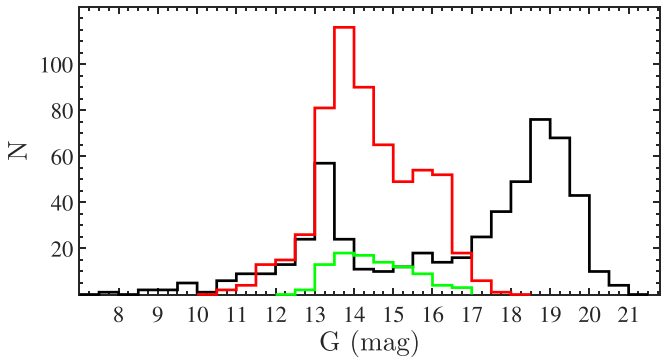

Figure 3. G magnitude distribution of Gaia DR2. The black and red histograms are the G magnitude distributions for 558 stars in the OFSC and 591 HiVelSCs, respectively, and the green one is for 92 conservative HiVelSCs introduced in Section 5.2. The red and greed distributions miss the second mode at the faint end of magnitude distribution of the OFSC because LAMOST is magnitude-limited (Sloan Digital Sky Survey r-band magnitude less than 17.8 mag; Du et al. 2018a).

stars in the OFSC. The red histogram is the distribution for 591 HiVelSCs, and the green one is for 92 conservative HiVelSCs introduced in Section 5.2. From this figure, we can clearly see that our HiVelSC sample contains relatively more objects in the magnitude range from 13–16.5 mag, and we miss the second mode at the faint end of magnitude distribution of the OFSC because LAMOST is magnitude limited.

Figure 4 shows the Hertzsprung–Russell diagram for 591 HiVelSCs (green and blue x-marks) and over 8 million "low-f"

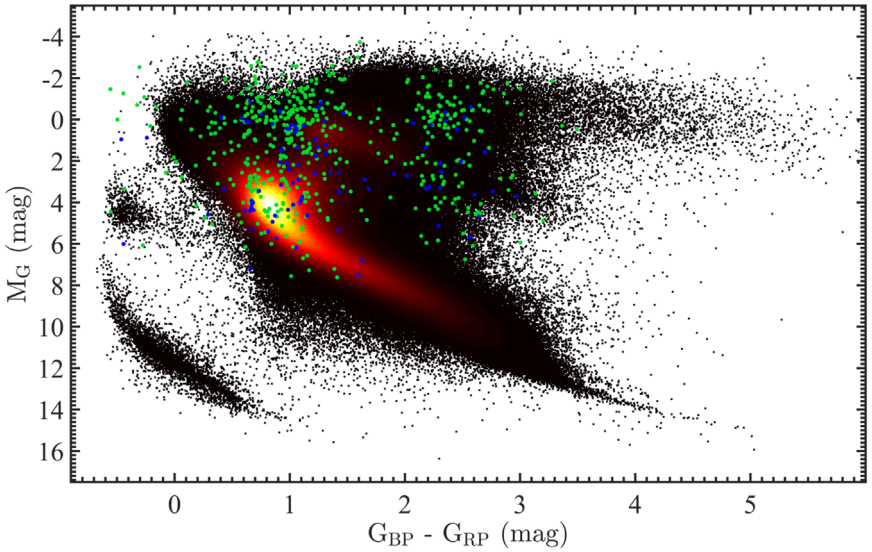

Figure 4. The Hertzsprung–Russell diagram for all the 591 HiVelSCs (green and blue x-marks), 92 of which are conservative HiVelSCs (blue x-marks) introduced in Section 5.2. The black solid dots represent over 8.48 million "low-f" spectra mentioned in Section 2.3.

spectra introduced in Section 2.3 (black solid dots). The *x*-axis represents the color index in the Gaia Blue Pass (BP) and Red Pass (RP) bands (BP–RP), and the *y*-axis gives the absolute magnitude of the Gaia *G* band. It should be noted that we do not consider extinction when construct the HR diagram, because of the caveats using the extinction in the *G* band for individual sources (Andrae et al. 2018). From this figure, we can see that the majority of 591 HiVelSCs are giant stars.

As mentioned in Section 2.3, seven Galactic potential models are used to estimate escape velocities for 591 HiVelSCs, and Table A1 lists these escape velocities for the 20 fastest HiVelSCs. In this table, $V_{\rm esc}$(W), $V_{\rm esc}$(G), $V_{\rm esc}$(Ke), $V_{\rm esc}$(Ko), $V_{\rm esc}$(P), $V_{\rm esc}$(M), and $V_{\rm esc}$(X) are escape velocities estimated by using the seven potential models of Watkins +2019, Gnedin+2005, Kenyon+2014, Koposov+2010, Paczynski+1990, MWPotential2014, and Xue+2008, respectively. Meanwhile, we estimate the probability $P_{\rm ub}$ of being unbound from the Milky Way, which is defined as the percentage of $V_{\rm GC}$ larger than escape velocity in 1000 MC realizations of $r_{\rm GC}$ and $V_{\rm GC}$, and Table A2 lists these probabilities for the 20 fastest HiVelSCs. In this table, $P_{\rm ub}$(W), $P_{\rm ub}$(G), $P_{\rm ub}$(Ke), $P_{\rm ub}$(Ko), $P_{\rm ub}$(P), $P_{\rm ub}$(M), and $P_{\rm ub}$(X) are unbound probabilities estimated by using the above seven potential models. Table 3 lists the number of HiVelSCs with $P_{\rm ub} > 50\%$ under each potential model, and we can see that at least 43 HiVelSCs have $P_{\rm ub} > 50\%$ of being unbound in the Watkins+2019 potential model, and at most 304 HiVelSCs have $P_{\rm ub} > 50\%$ of being unbound in the Xue+2008 potential model, and the amount of unbound HiVelSCs with $P_{\rm ub} > 50\%$ in other potential models is given by a number that is within the range (43–304), i.e., larger than 43 and less than 304.

To visually highlight possibly unbound HiVelSCs, we plot the total velocities in the Galactic rest frame $V_{\rm GC}$ as a function of Galactocentric distances $r_{\rm GC}$ for 591 HiVelSCs (black and red solid dots) in Figure 5, and also plot escape velocities at different $r_{\rm GC}$ with colored short dashed lines based on the above seven potential models. Considering the total velocity uncertainties, there are at least 43 stars in Figure 5 that can escape from the Galaxy in the most conservative Watkins +2019 potential model (resulting in the largest escaping velocities) with $P_{\rm ub} > 50\%$, and 287 stars are bound in the least conservative potential model of Xue+2008 (resulting in the smallest escaping velocities) with $P_{\rm ub} \leqslant 50\%$. Whether the remaining 261 stars are marginally unbound with $P_{\rm ub} > 50\%$ or not depends on the potential model used.

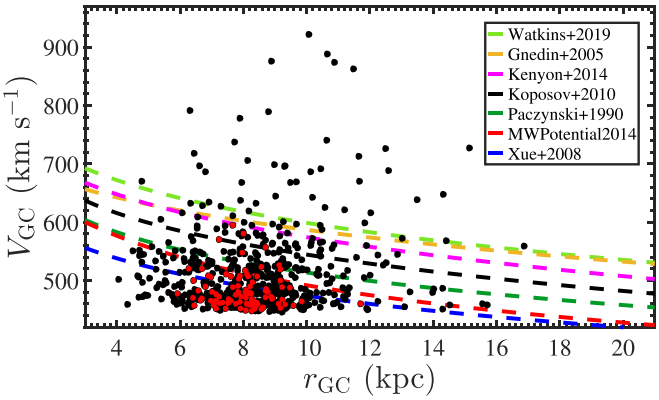

Figure 5. Total velocities in the Galactic rest frame ($V_{\rm GC}$) as a function of Galactocentric distances ($r_{\rm GC}$) for 591 HiVelSCs. The seven dashed curves in different colors are escape velocities at different distances $r_{\rm GC}$ determined by seven Galactic potential models (Paczynski 1990; Gnedin et al. 2005; Xue et al. 2008; Koposov et al. 2010; Kenyon et al. 2014; Bovy 2015; Watkins et al. 2019), and the black and red solid dots are 591 HiVelSCs, 92 of which are conservative HiVelSCs (red solid dots) introduced in Section 5.2.

In order to mark HiVelSCs with high quality Gaia astrometry, here we adopted equations (C.1), (C.2), and the latter two criteria of selection A in Appendix C of Lindegren et al. (2018), and the equality cuts from (i) to (iv) in Section 4 of Marchetti et al. (2019). The "astrometric_flag" column in Table 1 is used to determine the quality of astrometric parameters, and the value of "1" represents a HiVelSC that satisfies all above criteria. Using the "astrometric_flag" column, 476 HiVelSCs have conservative high-quality astrometric parameters of equatorial coordinates, parallaxes, and proper motions.

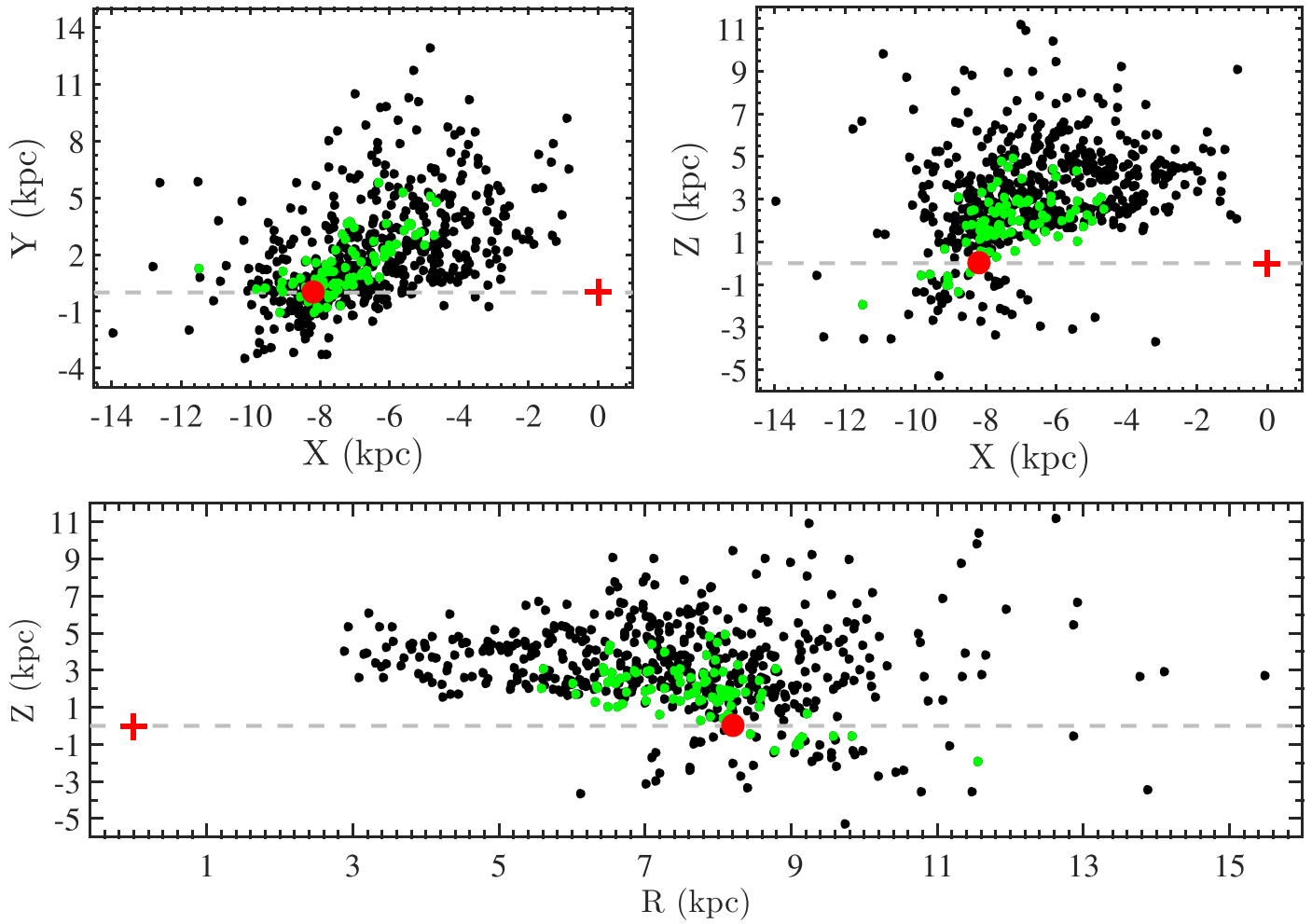

Figure 6. The spatial distribution of 591 HiVelSCs. Upper left panel: the distribution on the Galactic plane. Upper right panel: the distribution in the (X, Z) plane. Bottom panel: the distribution in the Galactocentric cylindrical coordinates (R, Z). The Sun and GC are marked by a red solid circle and a red plus, respectively. The black and green solid dots represent 591 HiVelSCs, and the green solid dots are 92 conservative HiVelSCs introduced in Section 5.2.

Table 3
The Number of HiVelSCs with Probabilities of Being Unbound Larger than 50% ($P_{\rm ub} \geqslant 50\%$) in Each of the Seven Potential Models

	Watkins+2019	Gnedin+2005	Kenyon+2014	Koposov+2010	Paczynski+1990	MWPotential2014	Xue+2008
$P_{\rm ub} \geqslant 50\%$	43	52	59	97	149	211	304

3. Properties of High-velocity Star Candidates

3.1. Distribution of Spatial Positions and Velocities

The spatial distribution of 591 HiVelSCs is shown in Figure 6. The upper panels are the distribution on the Galactic disk and the (X, Z) plane, and the bottom panel is the distribution in the Galactocentric cylindrical coordinates (R, Z). From the upper panels, we can see that all the 591 HiVelSCs are located on the side of the Sun having negative X, whereas the majority of them have positive Y (∼80.7%) and Z (∼91%). From the bottom panel, we note that about half (49%) of our HiVelSCs lie away from the stellar disk with $|Z| \geqslant 3$ kpc, which is the edge of the thick disk (Carollo et al. 2010).

Figure 7 shows the Galactocentric velocity components of our HiVelSCs, showing that they are not clumped in velocity. These stars show symmetry in the V_x–V_z plane but an obvious asymmetry in the V_x–V_y plane, and most of the HiVelSCs have negative values of V_y. There are at most 304 out of 591 HiVelSCs unbound to the Galaxy with $P_{\rm ub} > 50\%$ and 251 (∼82.6%) of them have negative values of V_y, assuming the Xue+2008 potential model. (The number of unbound ones is smaller if we assume other potential models.) Such an asymmetry in the V_x–V_y plane is consistent with the discussion in de la Fuente Marcos & de la Fuente Marcos (2019), and negative V_y components (retrograde) tend to be significantly larger than the positive counterparts (prograde). But this could be a side effect of the large uncertainties in heliocentric distances (Schönrich et al. 2011; de la Fuente Marcos & de la Fuente Marcos 2019). In order to further exclude stars with large uncertainties on distances, we use "astrometric_flag" to single out 245 stars with more conservative Gaia astrometry out of all 304 unbound HiVelSCs mentioned above, and 206 (∼84%) of them still have retrograde V_y. This result is consistent with that in de la Fuente Marcos & de la Fuente

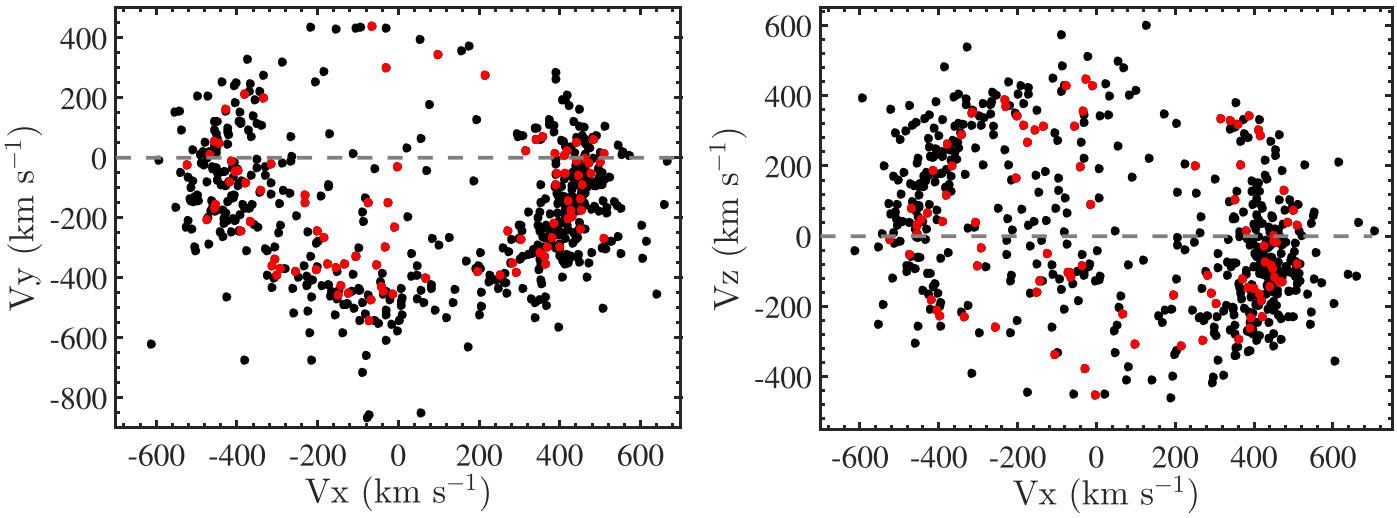

Figure 7. Galactocentric velocity distribution of 591 HiVelSCs. The black and red solid dots represent 591 HiVelSCs, and the red solid dots are 92 conservative HiVelSCs introduced in Section 5.2.

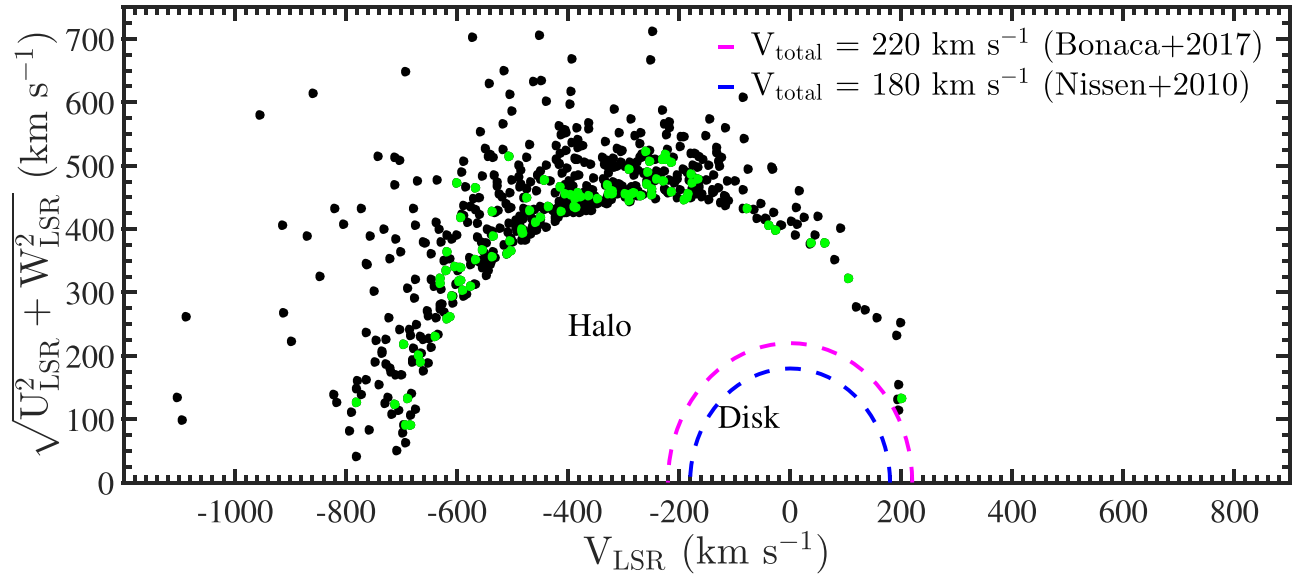

Figure 8. Toomre diagram for 591 HiVelSCs; (U_{LSR}, V_{LSR}, W_{LSR}) is the three-dimensional velocity with respect to the local rest frame. The magenta and blue dashed semicircles represent $V_{total} = \sqrt{U_{LSR}^2 + V_{LSR}^2 + W_{LSR}^2} = 220$ km s^{-1} and $V_{total} = \sqrt{U_{LSR}^2 + V_{LSR}^2 + W_{LSR}^2} = 180$ km s^{-1}, respectively, and they can be used to distinguish halo stars from disk stars. The black and green solid dots represent 591 HiVelSCs, and the green solid dots are 92 conservative HiVelSCs introduced in Section 5.2.

Marcos (2019), but the ratio of HiVelSCs with negative values of V_y is much higher. As discussed in literature (Cicone et al. 2016; de la Fuente Marcos & de la Fuente Marcos 2019; Marchetti et al. 2019), most unbound HiVelSCs having negative values of V_y suggest a population of high-velocity stars that may have an extragalactic provenance.

3.2. Halo or Disk Stars?

Figure 8 shows the Toomre diagram for 591 HiVelSCs, which has been widely used to distinguish the thin-disk, thick-disk, and halo stars. On the x-axis, we plot the component V_{LSR} of the space total velocity (V_{total}) with respect to the LSR, and on the y-axis the perpendicular component to it, $\sqrt{U_{LSR}^2 + W_{LSR}^2}$. The magenta and blue dashed semicircles are dividing lines between halo and disk stars, which were defined by Bonaca et al. (2017) and Nissen & Schuster (2010), respectively. The magenta dashed semicircle can be represented by $|V_{total}| \geqslant 220$ km s^{-1} (Bonaca et al. 2017), and the blue one can be defined as $|V_{total}| \geqslant 180$ km s^{-1} (Nissen & Schuster 2010). Here, we adopt the more conservative magenta dashed semicircle as the dividing line of halo and disk stars. As shown in this figure, all HiVelSCs are located outside of the magenta dashed semicircle, which means that all the 591 HiVelSCs have halo-like kinematic properties.

Following Bensby et al. (2003), we estimate the relative probabilities for the thick-disk-to-halo membership using their Equations (1)–(3), which can also be used to distinguish stellar population, and the result shows that relative probabilities of all 591 HiVelSCs of not being halo stars are far less than 0.1 and nearly equal to 0. Such a result indicates that all the 591

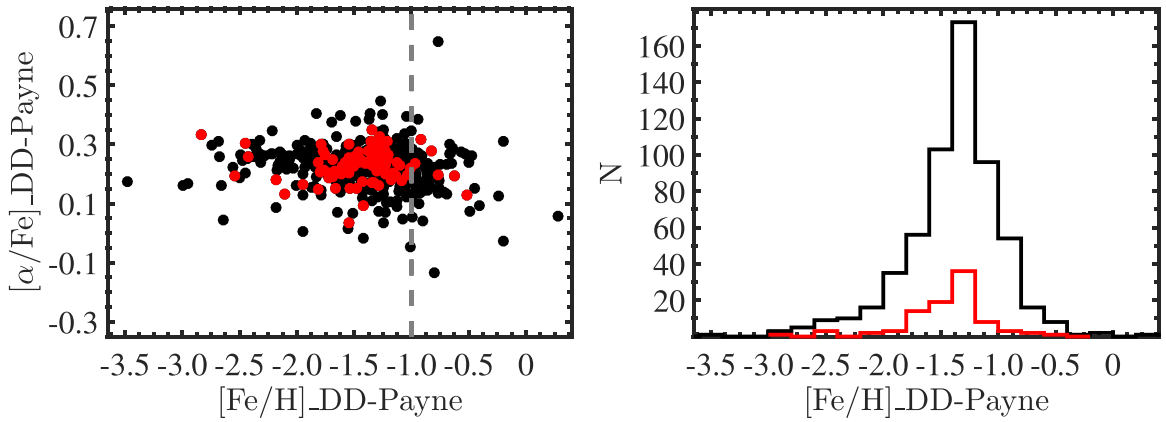

Figure 9. Left panel: the distribution of 591 HiVelSCs on the ([α/Fe], [Fe/H]) plane. The horizontal and vertical axes are the metallicity ([Fe/H]_DD-Payne) and the α element abundance ([α/Fe]_DD-Payne), respectively, and they are estimated by the DD-Payne method. Right panel: the distribution of [Fe/H]_DD-Payne for 591 HiVelSCs, which peaks at about [Fe/H] ~ -1.2 and has a wide range from near [Fe/H] ~ -3.5 to [Fe/H] $\sim +0.5$. The black and red solid dots in the left panel represent 591 HiVelSCs, and the red solid dots are 92 conservative HiVelSCs introduced in Section 5.2. The black histogram is the distribution of [Fe/H]_DD-Payne for 591 HiVelSCs, and the red one is the distribution of [Fe/H]_DD-Payne for 92 conservative HiVelSCs.

HiVelSCs are halo stars with extremely high probabilities, and it is consistent with the result obtained by using the Toomre diagram.

Besides the kinematic methods, chemistry is usually used together with kinematics to study the stellar population and possible origin places, and we use the data-driven Payne method (DD-Payne) described in Xiang et al. (2019) (see also Ting et al. 2017) to determine α element abundance ([α/Fe]) in this work, since it was not provided by the LASP. The DD-Payne method also provides atmospheric parameters for 591 HiVelSCs, and these parameters are included in our "LAMOSTDR7-GAIADR2-HiVelSC" catalog together with LASP atmospheric parameters. Table A3 shows these parameters for the 20 fastest HiVelSCs, where $T_{\rm eff}$_LASP, log g_LASP, and [Fe/H]_LASP are atmospheric parameters determined by the LASP, and $T_{\rm eff}$_DD-Payne, log g_DD-Payne, [Fe/H]_DD-Payne and [α/Fe]_DD-Payne are parameters obtained by the DD-Payne method.

The left panel of Figure 9 plots the distribution of 591 HiVelSCs on the DD-Payne (α, [Fe/H]) plane, and the mean and standard deviation of the α-abundances of our HiVelSCs are about +0.23 and 0.07 dex. This is consistent with the results in Du et al. (2018b) and Hawkins et al. (2015), which have mean α abundances of $\alpha = +0.22$ dex and $\alpha = +0.24$ dex, respectively. The right panel shows the [Fe/H]_DD-Payne distribution of these stars, which peaks at near [Fe/H] ~ -1.2 and has a wide range from near [Fe/H] ~ -3.5 to [Fe/H] $\sim +0.5$. From this figure, the 591 kinematically selected halo stars are mostly metal-poor and slightly α-enhanced. In addition, their [Fe/H] distribution and its peak value at about [Fe/H] ~ -1.2 are consistent with the distribution of inner halo stars in Conroy et al. (2019) and Liu et al. (2018). While the mean or peak values of metallicity distributions of the inner halo in some research works (Carollo et al. 2007, 2010; An et al. 2013; Allende Prieto et al. 2014; Xue et al. 2015; Das & Binney 2016; Zuo et al. 2017; Mackereth et al. 2019; Youakim et al. 2020) can shift toward more metal-poor for several reasons, such as bias in the halo stars selection as discussed in Conroy et al. (2019), the metallicity distribution of our 591 HiVelSCs is nonetheless broadly consistent with that of the inner halo in these works.

As mentioned in recent works (Bonaca et al. 2017; Du et al. 2018a; Conroy et al. 2019), a fraction of kinematically defined metal-rich halo stars are in situ components of the local stellar halo, which display thick-disk chemistry on halo-like orbits and are confined to the range of $|z| \leqslant 10$ kpc and $R_{\rm gal} \leqslant 20$ kpc. Such in situ halo stars are considered to be formed in the initial collapse of the Milky Way or formed in the disk or bulge and are subsequently kinematically heated (Bonaca et al. 2017; Du et al. 2018a; Conroy et al. 2019). In our 591 HiVelSCs, 83 (∼14%) of them are metal-rich halo stars with $[{\rm Fe/H}]_{\rm DD-Payne} > -1$, and their vertical height and Galactocentric radius are limited in the range of $|z| \leqslant 10$ kpc and $R_{\rm gal} \leqslant 20$ kpc. Thus, they may be the in situ halo stars (Nissen & Schuster 2010; Conroy et al. 2019), and such a lower ratio of about 14% (but 30% from Du et al. 2018a and 50% from Bonaca et al. 2017) is consistent with the result in Conroy et al. (2019) that the bulk of the stellar halo formed from accretion and tidal disruption.

In recent studies of the Galactic halo's metallicity distribution (Zuo et al. 2017; Liu et al. 2018; Conroy et al. 2019), the majority of the retrograde stars are more metal-poor than the prograde stars. We thus divide our HiVelSCs into two groups, i.e., prograde and retrograde HiVelSCs, and plot their distribution on the ([Fe/H], R) plane in the upper panels of Figure 10. We further divide them into another two types, i.e., metal-rich ([Fe/H] > -1) and metal-poor ([Fe/H] $\leqslant -1$) HiVelSCs, and plotted them on the (V_y, R) plane in the bottom panels. In this figure, we show the mean values of the horizontal and vertical axes as red solid dots.

From the upper panels, we can see that retrograde HiVelSCs have a slightly low mean value of [Fe/H] ($\langle$[Fe/H]$\rangle = -1.4$), and this is consistent with the results in the above literature (Zuo et al. 2017; Liu et al. 2018; Conroy et al. 2019). In the bottom panels, about 75% of the metal-rich HiVelSCs are retrograde, and the ratio for metal-poor HiVelSCs is about 80%. Thus, the majority of our HiVelSCs tend to be retrograde no matter if they are metal-rich or metal-poor. From the bottom panels, we can see that metal-poor HiVelSCs tend to have significantly faster mean retrograde velocities V_y($\langle V_y \rangle = -186$ km s^{-1}). Although the results here combining chemistry and kinematics are consistent with recent studies, further verification is needed because the

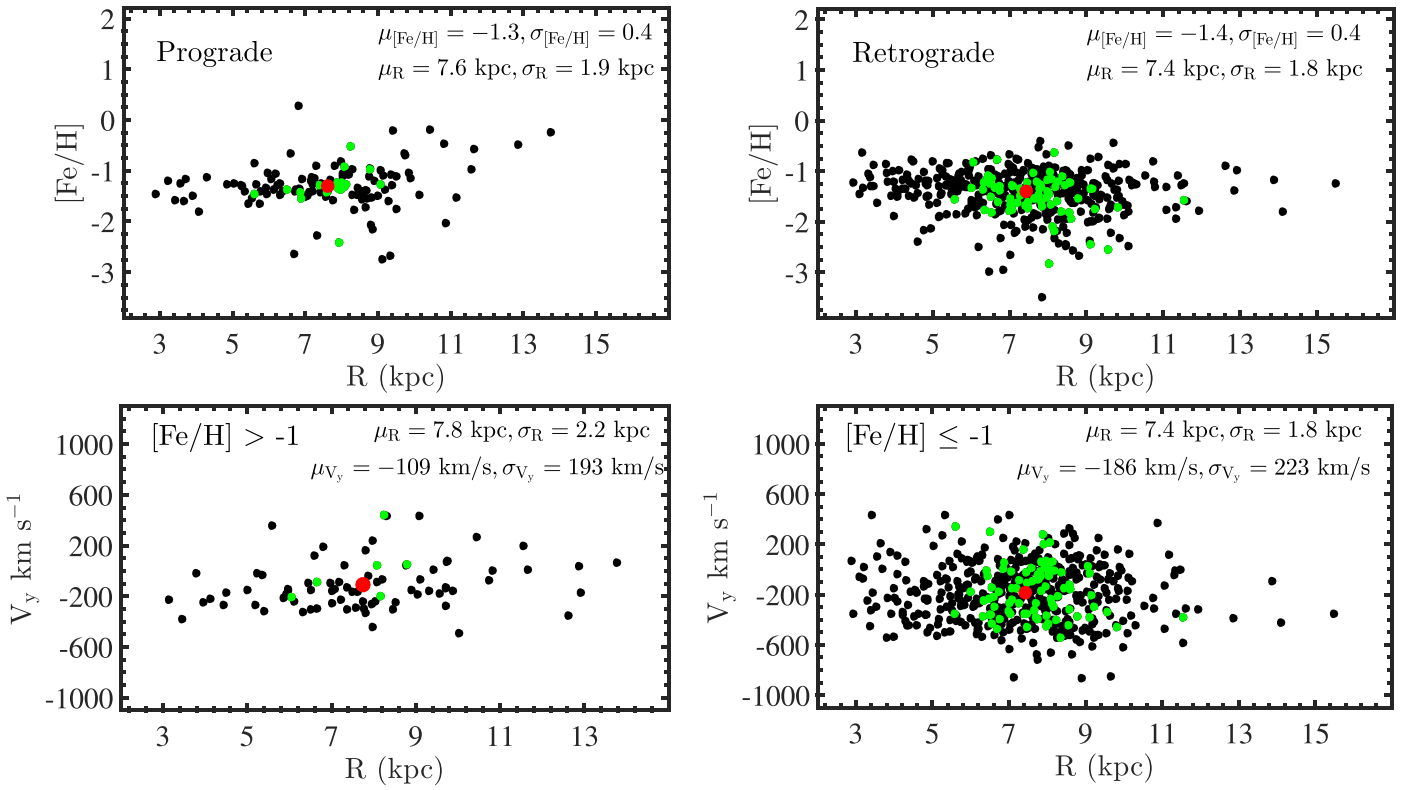

Figure 10. Upper panels: metallicity ([Fe/H]) vs. Galactocentric radius (R) separated according to the y-components (V_y) of the Galactocentric total velocities. The red solid dot marks the mean values of [Fe/H] and R. The upper left and right panels are for prograde and retrograde HiVelSCs, respectively. Bottom panels: distribution of 591 HiVelSCs on the (V_y, R) plane separated by [Fe/H]. The red solid dot marks the mean values of V_y and R. The bottom left and right panels are for HiVelSCs with [Fe/H] > -1 and [Fe/H] $\leqslant -1$, respectively. The green solid dots in each panel represent 92 conservative HiVelSCs introduced in Section 5.2.

number of stars in our HiVelSC samples is small and the precisions for chemical and kinematic parameters need further improvement, especially the precisions that correspond to the metallicity and RV from LAMOST low-resolution spectra, as well as those of parallaxes and proper motions from Gaia DR2.

4. Orbital Integration and Origin

In order to better understand the ejection locations of our HiVelSCs, we perform numerical orbit integrations and trace their trajectories back in time using the python package Galpy (Bovy 2015). For each star, we perform 1000 random MC samplings of the equatorial coordinates, RV, proper motion, and parallax considering the measurement errors as discussed in Section 2.2, and trace each orbit back to 10 Gyr ago, with a fixed time step of 10 Myr, using the MWPotential2014 potential of the Galpy package which consists of a bulge modeled as a power-law density profile that is exponentially cut off, a MiyamotoNagaiPotential disk, and a Navarro–Frenk–White dark-matter halo (Bovy 2015).

We estimate for each HiVelSC the maximum distance above the Galactic plane (Z_{max}), the eccentricity (e), the minimum crossing radius (r_{min}), and the energy (E) of each orbit during the 1000 MC realizations, record the Galactocentric coordinates (x_c, y_c) at the instant when $z = 0$, and define the crossing radius (r_c) as $r_c = \sqrt{x_c^2 + y_c^2}$ (Marchetti et al. 2019). In the case of multiple disk crossings for each orbit, r_{min} is defined as the minimum r_c. In order to determine unbound or bound orbits, we calculate the energy of $E - \Phi(\infty)$, in which E is the orbit energy and $\Phi(\infty)$ is the energy of the convergence potential MWPotential2014 at infinity.

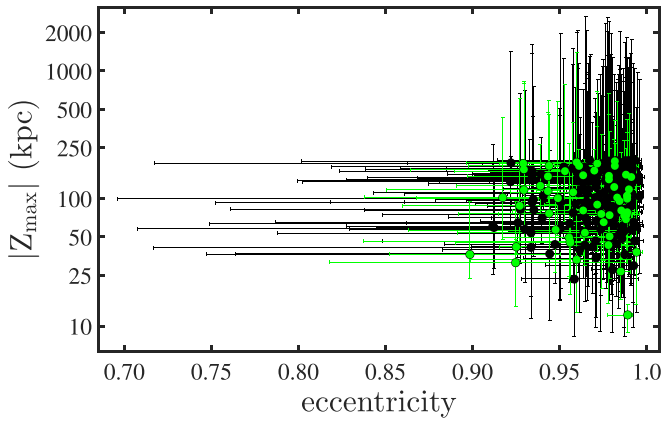

Figure 11. The maximum height above the Galactic plane $|Z_{max}|$ as a function of eccentricity e; the y-axis is in log scale. The black solid dots represent 246 bound HiVelSCs with $Z_{max} \leqslant 200$ kpc, and the green solid dots represent 55 conservative HiVelSCs with $Z_{max} \leqslant 200$ kpc. The conservative HiVelSCs are introduced in Section 5.2.

In Figure 11, we plot Z_{max} as a function of e only for 246 bound HiVelSCs with $Z_{max} \leqslant 200$ kpc, solid dots show the median values of Z_{max} and e, and the error bars mark their standard deviations. This plot has the ability to sort out stars of similar orbits like the Toomre diagram, because eccentricity e represents the shape of the orbit and Z_{max} represents the amplitude of the orbit vertical oscillation (Boeche et al. 2013). From this figure, we can see that the range of e and Z_{max} are [0.898, 0.996] and [12 kpc,

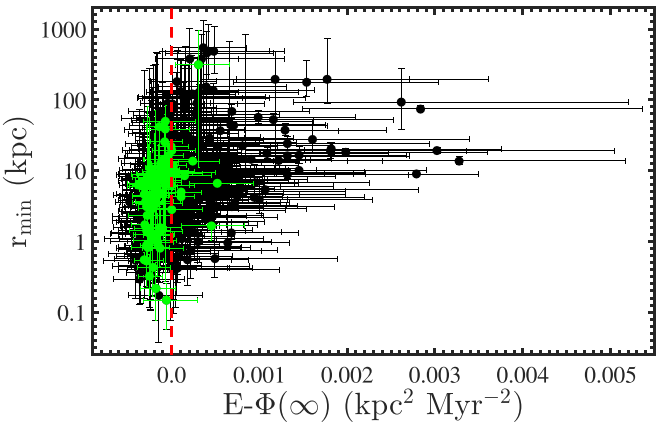

Figure 12. Minimum crossing radius r_{min} as a function of energy $E - \Phi(\infty)$; the y-axis is in log scale. The dashed red line separates unbound ($E - \Phi(\infty) > 0$) from bound ($E - \Phi(\infty) < 0$) orbits. The black and green solid dots are 591 HiVelSCs, and the green solid dots represent 92 conservative HiVelSCs introduced in Section 5.2.

Table 4
The Classification Criteria of HiVelSCs

Class	P_{gc}	P_{MW}	P_{ub}
HVS candidates	>0.16	···	···
HRS candidates	<0.16	>0.5	>0.5
RS candidates	<0.16	>0.5	<0.5
OUT candidates	<0.16	<0.5	···

200 kpc], respectively, and the median values of e and Z_{max} are 0.978 and 105 kpc, respectively. These results show that the 246 HiVelSCs stars are on highly eccentric orbits, and all of them have e above 0.6 and $Z_{max} > 3$ kpc, which indicates that they are kinematically consistent with the halo population (Boeche et al. 2013; Kordopatis et al. 2013a, 2013b; Hawkins et al. 2015). Table 2 lists e, Z_{max}, r_{min}, and $E - \Phi(\infty)$ in the last four columns, and Table A4 explains the four orbit parameters in detail. For unbound HiVelSCs and bound HiVelSCs with $Z_{max} > 200$ kpc, Tables 2 and A4 does not provide e and Z_{max}.

In Figure 12, we plot r_{min} as a function of the energy $E - \Phi(\infty)$, and the red dashed line is the separation region between bound and unbound HiVelSCs. In this figure, there are 240 (41%) HiVelSCs with remarkably high values of the energy and traveling on unbound orbits ($E - \Phi(\infty) > 0$).

After tracing the orbit back, we derive the origins of 591 HiVelSCs from the positions of these stars crossing the disk (Marchetti et al. 2019). Using the minimum crossing radius r_{min}, we obtain the probability that a star is ejected from the GC (P_{gc}), which is defined as the fraction of orbits with $r_{min} < 1$ kpc in 1000 MC orbits, and the probability that a star is ejected from the Galaxy (P_{MW}), which is defined as the fraction of orbits with $r_{min} < 25$ kpc (Xu et al. 2015; Du et al. 2018b, 2019). Using P_{gc}, P_{MW}, and the unbound probability of P_{ub} defined in Section 2.4, the HiVelSCs are divided into four types, and the classified criteria are shown in Table 4. In this table, "HVS" represents the fastest hypervelocity stars in the Galaxy; "HRS" represents hyper-runaway stars; "RS" represents the runaway stars; and "OUT" represents fast halo stars. In our "LAMOSTDR7-GaiaDR2-HiVelSC" catalog, the column "Origin_Class" records the result of this classification, and the last column of the Table A2 lists the classification results for the 20 fastest HiVelSCs. Following the classification criteria in Table 4, our HiVelSCs are divided into 91 HVS candidates, 107 HRS candidates, 221 RS candidates, and 172 OUT candidates. The HVS and OUT candidates are considered to be stripped from the GC and dwarf galaxies, respectively, and both HRS and RS stars were ejected from the Galactic disk.

The origins of our HiVelSCs from tracing back their orbits might suggest that a fraction (71%) of them were ejected from the Galactic disk or bulge, and others originated from dwarf galaxies. This appears to be in contradiction with that inferred from the metallicities of these HiVelSCs, i.e., only a small fraction (14%) of HiVelSCs originated from the Galactic disk or bulge, as explained in Section 3.2. The main reason for such a difference is that although the orbits of these stars can cross the Galactic disk or bulge, it does not necessarily mean that they must be ejected from the disk or bulge. Besides, uncertainties of kinematic parameters and the selection of the Galactic potential model will affect the orbits.

In Figure 13, we plot the distribution of P_{gc}, P_{MW}, and P_{ub} for HVS, HRS, RS, and OUT candidates, respectively. In the upper left panel, most HVS candidates are located in the region with $P_{gc} \leqslant 0.5$, $P_{ub} \leqslant 0.5$, and $P_{MW} > 0.5$, and this implies that our criterion might be too optimistic in the sense that we might overestimate the number of HVS stars. A fraction of HVS candidates will be proved to be one of the other three types of stars (HRS, RS, or OUT stars). A similar conclusion can be drawn from other the three panels of this figure, which indicates that the classification criteria in Table 4 used in this work and in other literature (Du et al. 2018b, 2019; Marchetti et al. 2019) might not be sufficient to determine the origin places of our HiVelSCs. In the near future, more precise measurements of atmospheric parameters (in particular the metallicity, parallax, proper motions, and improved Galactic potential models) will be available, and a detailed orbit analysis to further investigate the origin places for our HiVelSCs will be carried out as needed.

5. Discussion

5.1. The Zero-point Correction of Parallax

In this section, we discuss the impact of a −0.029 mas global parallax zero-point mentioned in Lindegren et al. (2018) for 591 HVCSs, derived from distant quasars. Being a negative offset, it leads to lower inferred distance, and therefore smaller total velocity. We repeat the calculations described in Section 2.2 but using the mean vector $m = [\alpha, \delta, \varpi + \varpi_{zp}, \mu_{\alpha*}, \mu_\delta]$ to estimate Galactocentric distance and total velocity, where $\varpi_{zp} = 0.029$ mas.

After such a parallax zero-point correction, both Galactocentric distances r_{GC} and total velocities V_{GC} are reduced for 591 HiVelSCs. The maximum, minimum, and mean value of r_{GC} reduction are 4.0 kpc, 0.2 pc, and 0.4 kpc, respectively, and those of V_{GC} reduction are 241 km s^{-1}, 0.15 km s^{-1}, and 66 km s^{-1} respectively. Unbound probabilities in the seven potential models mentioned in Section 2.4 are also reestimated, and we find that the number of unbound HiVelSCs in the Watkins+2019 potential model with $P_{ub} \geqslant 50\%$ decreased from 43 to 8, the number of bound HiVelSCs with $P_{ub} < 50\%$ in the Xue+2008 potential model increased from 284 to 492,

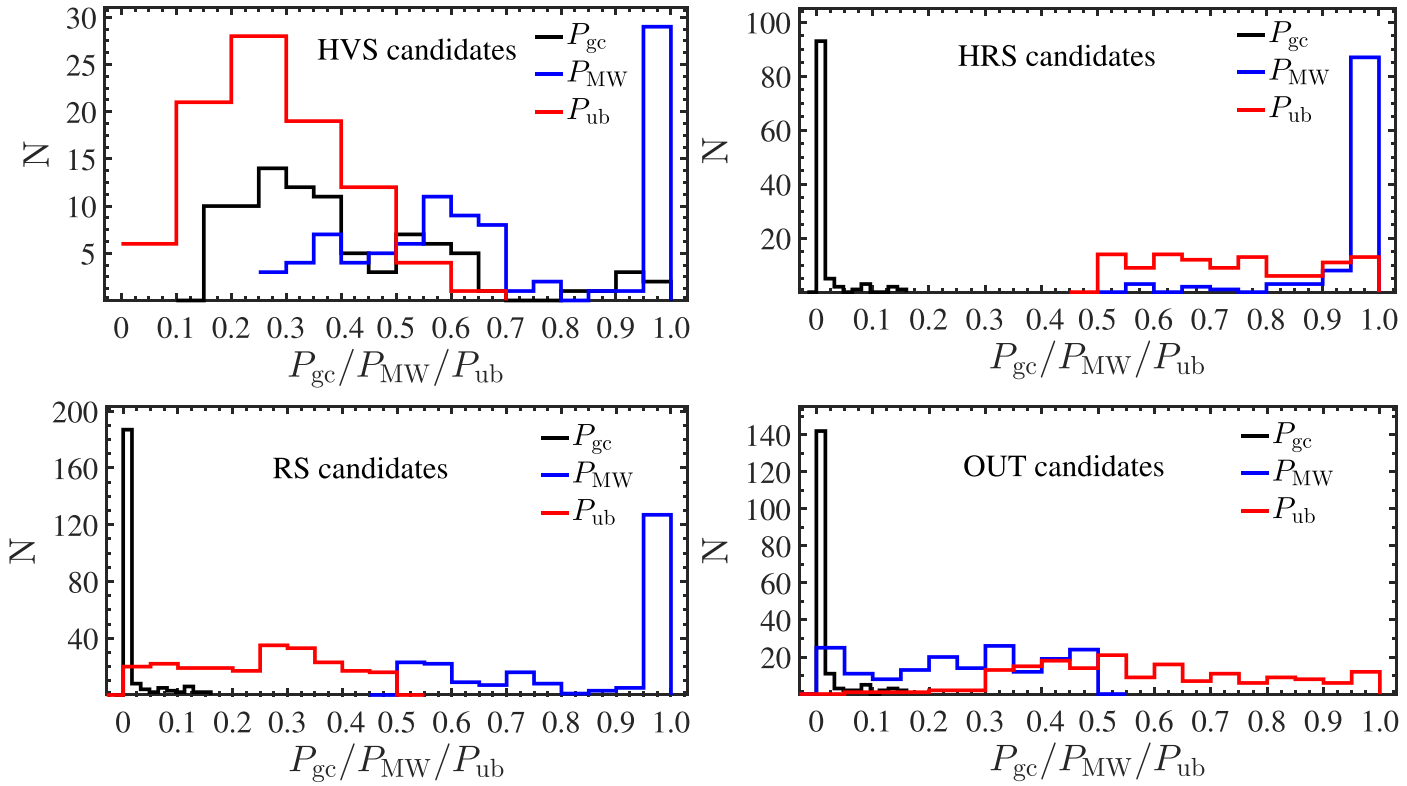

Figure 13. The distribution of probability that a star is ejected from the GC (P_{gc}), probability that a star is ejected from the Galaxy (P_{MW}), and unbound probability (P_{ub}) for hypervelocity stars ("HVS"), hyper-runaway stars ("HRS"), runaway stars ("RS"), and fast halo stars ("OUT"), respectively. P_{gc} and P_{MW} are defined in Section 4, and P_{ub} is defined in Section 2.4.

Table 5
The Results Using More Stringent Selection Criteria

Criteria[a]	N1[b]	N2[c]	N3[d]	N4[e]	Maximum V_{GC}[f] (km s^{-1})
Only criteria mentioned in Section 2.3 used	591	43	304	287	922
Astrometric_flag = 1	476	34	245	231	888
$f_{\varpi} = \sigma_{\varpi}/\varpi \leqslant 0.1$	120	2	38	82	876
$\sigma_{V_{GC}}/V_{GC} \leqslant 0.2$	247	3	87	160	876
Above criteria are all used	92	0	26	66	595

Notes.
[a] Selection criteria. The criteria from the second to fifth rows are adopted after using the criteria in the first row.
[b] Total number of HiVelSCs satisfied the selection criteria listed in the first column.
[c] The number of HiVelSCs unbound in the Watkins+2019 potential model with $P_{ub} \geqslant 50\%$.
[d] The number of HiVelSCs unbound in the Xue+2008 potential model with $P_{ub} \geqslant 50\%$.
[e] The number of HiVelSCs bound in the Xue+2008 potential model with $P_{ub} < 50\%$.
[f] The maximum Galactocentric velocities for all HiVelSCs selected by the criteria in the first column.

and whether the other 99 HiVelSCs are unbound with $P_{ub} \geqslant 50\%$ or not depended on the potential model used.

5.2. Selecting HiVelSCs with More Conservative Criteria

In Section 2.3, we describe the selection criteria of 591 HiVelSCs, and here we focus on more stringent selection criteria and show the corresponding results in Table 5. The first column of each row in this table lists the selection criteria, and the second to sixth columns show the corresponding results of using these criteria, which are the total number ($\leqslant$591) of the HiVelSCs, the number of HiVelSCs unbound in the Watkins +2019 potential model with $P_{ub} \geqslant 50\%$, the number of HiVelSCs unbound in the Xue+2008 potential model with $P_{ub} \geqslant 50\%$, the number of HiVelSCs bound in the Xue+2008 potential model with $P_{ub} < 50\%$, and the maximum value of total Galactocentric velocities for HiVelSCs selected by the criteria in the first column, respectively. As a comparison, the results using the selection method in Section 2.3 are listed in the first row, and the results using other more conservative criteria are listed from the second to fifth rows.

From the second row of Table 5, we can see that 476 HiVelSCs have conservative high-quality astrometric parameters, i.e., astrometric_flag = 1, and 34 of them are still unbound in the Watkins+2019 potential model with $P_{ub} \geqslant 50\%$. If we focus on HiVelSCs with more precise parallaxes, from the third row we can see that only 120 HiVelSCs satisfy this criteria, and only two of them are unbound in the Watkins+2019 potential model with $P_{ub} \geqslant 50\%$. If we focus on HiVelSCs with more precise total velocities V_{GC}, from the fourth row we can see that only 247 HiVelSCs are left, and three of them are unbound in the Watkins+2019 potential model with $P_{ub} \geqslant 50\%$.

Finally, if we use all criteria listed in the first column from the second to fourth rows, we can see in the fifth row that only 92 HiVelSCs are left, and none of them are unbound in the Watkins+2019 potential model with $P_{ub} \geqslant 50\%$, but there are 26 HiVelSCs unbound in the Xue+2008 potential model with $P_{ub} \geqslant 50\%$. In Figures 2–12, we also show the distribution of

92 conservative HiVelSCs. Besides, in our "LAMOSTDR7-GAIADR2-HiVelSC" catalog, the "conservative_result" column is used to select the 92 conservative HiVelSCs by using "conservative_result = 1."

6. Conclusion

In this paper, we cross-match LAMOST DR7 with Gaia DR2 to find more high-velocity stars, and obtain a catalog consisting of over 10 million spectra (LAMOST-Gaia). Galactocentric distances r_{GC} and total velocities V_{GC} are estimated for over 8.48 million "low-f" entries in the LAMOST-Gaia catalog, which have positive Gaia parallax and low fractional parallax errors ($f_{\varpi} = \sigma_{\varpi}/\varpi \leqslant 0.2$). We define our sample of high-velocity stars as those who can escape from the Galaxy in at least one of the seven Galactic potential models adopted in this work, or have total velocities in the Galactic rest frame larger than 450 km s^{-1}, and this results in a total of 591 high-velocity star candidates (HiVelSCs) found from the LAMOST-Gaia catalog. Their total velocities V_{GC} are then recalculated using the radial velocities determined by the LAMOST Stellar Parameter Pipeline (LASP), because their RV uncertainties given by the LASP not only consider the calculation error caused by the LASP algorithm but also take into account the error introduced from the process of spectra observation and data processing. After the recalculation, the total velocities for all HiVelSCs are still >445 km s^{-1}, and our main conclusions are:

(i) Among 591 HVCs, the majority of them are giant stars, and 14 of them have been already collected in the Open Fast Stars Catalog (OFSC; Boubert et al. 2018). In this paper, we construct a catalog of "LAMOSTDR7-GAIADR2-HiVelSC" to collect parameters for 591 HiVelSCs, including 93 columns such as LAMOST radial velocity, atmospheric parameters, and five Gaia astrometry parameters, and 476 HiVelSCs have conservative high-quality astrometric parameters of Gaia DR2, which satisfy the criteria introduced in Section 2.4.

(ii) Using seven Galactic potential models, 43 HiVelSCs can escape from the Galaxy with unbound probabilities of $P_{ub} > 50\%$ in the potential model of Watkins et al. (2019) (Watkins+2019; resulting in the largest escaping velocities), 304 HiVelSCs are unbound in the potential model of Xue et al. (2008) (Xue+2008; resulting in the smallest escaping velocities) with $P_{ub} > 50\%$, and other 287 HiVelSCs are bound in the Xue+2008 potential model with $P_{ub} \leqslant 50\%$. As mentioned in Lindegren et al. (2018) and Arenou et al. (2018), there is a negative zero-point for Gaia parallax, and we attempt to correct the zero-point of −0.029 for 591 HiVelSCs, which leads to a decrease in the number of HiVelSCs unbound in the Watkins+2019 potential model with $P_{ub} > 50\%$, from 43 to 8. At the end of this work, we also discuss the effect if more conservative criteria are adopted to select HiVelSCs. The conclusion is that there are, in total, 92 HiVelSCs satisfying all of the three more conservative selection criteria, and they are referred to as 92 conservative HiVelSCs in the main text. Among them, there is no HiVelSCs unbound in the Watkins+2019 potential model with $P_{ub} > 50\%$ when all criteria listed in Table 5 are used, but there are 26 HiVelSCs having a $P_{ub} > 50\%$ of being unbound in the Xue+2019 potential model, and the maximum value of Galactocentric velocities V_{GC} for 92 conservative HiVelSCs is 595 km s^{-1}.

(iii) Using the Toomre diagram, probabilities for the thick-disk-to-halo and the distribution on the (eccentricity, z_{max}) plane, we find that all 591 HiVelSCs are kinematically associated with the halo population, which confirms the assumptions adopted in previous works that high-velocity stars in the solar vicinity mostly belong to the halo (Schuster & Nissen 1988; Ryan & Smith 2003; Schuster et al. 2006). The 591 HiVelSCs have a mean α abundance of $\alpha = +0.22$ dex, and their metallicities [Fe/H] peak at near [Fe/H] ~ -1.2 and have a wide range from near [Fe/H] ~ -3.5 to [Fe/H] $\sim +0.5$, which also indicates that on the whole they are metal-poor slightly α-enhanced inner-halo stars.

Among the 591 HiVelSCs, about 14% of them are metal-rich halo stars with [Fe/H] > -1, and they may be the in situ halo stars (Nissen & Schuster 2010; Conroy et al. 2019). These in situ halo stars are considered to be formed in the initial collapse of the Milky Way or formed in the disk or bulge and be subsequently kinematically heated (Bonaca et al. 2017; Du et al. 2018a; Conroy et al. 2019), and the low ratio of them indicates that the bulk of the stellar halo formed as a consequence of the accretion and tidal disruption processes as mentioned in Conroy et al. (2019).

(iv) Considering both their kinematics and chemistries, we find that most of our HiVelSCs have retrograde velocities of V_y, and retrograde HiVelSCs have a slightly lower mean value of [Fe/H], which is consistent with the results in the literature (Zuo et al. 2017; Liu et al. 2018; Conroy et al. 2019), meanwhile metal-poor ([Fe/H] < -1) HiVelSCs tend to have faster mean retrograde velocities V_y.

(v) There are 304 HiVelSCs unbound in the Xue+2008 potential model with $P_{ub} > 50\%$, and most of them move on retrograde ($V_y < 0$) orbits, which means, as it has been suggested in the literature, that a population of unbound stars may have an extragalactic provenance (Cicone et al. 2016; de la Fuente Marcos & de la Fuente Marcos 2019; Marchetti et al. 2019). In order to further investigate their origin, we track the orbits of 591 HiVelSCs back in time, and they are divided into four types, i.e., HVS, HRS, RS and OUT, according to their unbound probabilities (P_{ub}), and the probabilities of being ejected from the GC (P_{gc}) and Galactic disk (P_{MW}). We find that ∼15% of stars are from the GC, ∼55% of stars are from the Galactic disk, and ∼30% of stars have extragalactic origins, but we caution that due to the uncertainty in the phase-space measurement, further investigation is needed to confirm their origins.

We would like to thank an anonymous referee for helpful comments and suggestions. We thank Bovy Jo, Fu Xiao-Ting, Du Bing, Yan Hong-Liang, Shi Jian-Rong, Hou Wen, Chen Jian-Jun, Yuan Hai-Long, Guo Yan-Xin, Xue Xiang-Xiang, and Zhang Lan for helpful discussions. This work is supported by Chinese Space Station Telescope (CSST) pre-research projects of *Key Problems in Binaries* and *Chemical Evolution of the Milky Way and its Nearby Galaxies*, the National Key R&D Program of China (No. 2019YFA0405502), the National

Natural Science Foundation of China (Nos. U1931209, 11873056, 11991052, 11988101, 11890694, 11673058, and 11873016), and the National Key Program for Science and Technology Research and Development (grant No. 2016YFA0400704), Cultivation Project for LAMOST Scientific Payoff and Research Achievement of CAMS-CAS, and the key research program of frontier sciences, CAS (No.ZDBS-LY-7005). Y.S.T. is supported by the NASA Hubble Fellowship grant HST-HF2-51425.001 awarded by the Space Telescope Science Institute. Guoshoujing Telescope (the Large Sky Area Multi-Object Fiber Spectroscopic Telescope, LAMOST) is a National Major Scientific Project built by the Chinese Academy of Sciences. Funding for the project has been provided by the National Development and Reform Commission. LAMOST is operated and managed by the National Astronomical Observatories, Chinese Academy of Sciences.

Appendix
Tables

Here, we list four tables. Tables A1 and A2 list escape velocities $V_{\rm esc}$ and unbound probabilities $P_{\rm ub}$ (defined in Section 2.4) for the 20 fastest HiVelSCs in the seven potential models (Paczynski 1990; Gnedin et al. 2005; Xue et al. 2008; Koposov et al. 2010; Kenyon et al. 2014; Bovy 2015; Watkins et al. 2019) mentioned in Section 2.4, and Table A3 lists their atmospheric parameters (effective temperature $T_{\rm eff}$, surface gravity $\log g$, and metallicity [Fe/H]) and α element abundances ([α/Fe]). As mentioned in Section 2.4, we construct the catalog of "LAMOSTDR7-GAIADR2-HiVelSC" including 93 columns to list various parameters for 591 HiVelSCs, and Table A4 explains each column of this table in detail. The complete catalog is available in the China-VO PaperData Repository at doi:10.12149/101038.

Table A1
Escape Velocities of the 20 Fastest HiVelSCs in the Seven Galactic Potential Models

ID	$r_{\rm GC}$[a] (kpc)	$V_{\rm GC}$[a] (km s^{-1})	$V_{\rm esc}$(W)[b] (km s^{-1})	$V_{\rm esc}$(G)[b] (km s^{-1})	$V_{\rm esc}$(Ke)[b] (km s^{-1})	$V_{\rm esc}$(Ko)[b] (km s^{-1})	$V_{\rm esc}$(P)[b] (km s^{-1})	$V_{\rm esc}$(M)[b] (km s^{-1})	$V_{\rm esc}$(X)[b] (km s^{-1})
Hivel1	$10.1^{+0.9}_{-0.6}$	922^{+168}_{-136}	598	587	573	543	512	491	474
Hivel2	$10.6^{+0.6}_{-0.4}$	888^{+197}_{-142}	595	585	570	542	511	486	469
Hivel3	$8.9^{+0.1}_{-0.0}$	876^{+81}_{-73}	615	601	590	567	533	503	483
Hivel4	$10.9^{+0.8}_{-0.5}$	874^{+247}_{-168}	593	584	568	540	509	484	468
Hivel5	$11.5^{+1.6}_{-0.9}$	862^{+242}_{-147}	585	579	561	530	501	479	464
Hivel6	$6.3^{+0.8}_{-0.4}$	791^{+199}_{-142}	634	617	610	576	544	535	508
Hivel7	$8.8^{+0.4}_{-0.2}$	789^{+194}_{-126}	611	598	586	557	525	504	484
Hivel8	$7.9^{+0.0}_{-0.0}$	778^{+81}_{-69}	624	608	600	573	540	514	492
Hivel9	$10.6^{+1.7}_{-1.0}$	741^{+236}_{-156}	592	583	568	537	507	486	469
Hivel10	$7.7^{+0.3}_{-0.1}$	737^{+174}_{-114}	623	606	599	569	537	516	493
Hivel11	$15.2^{+2.0}_{-1.2}$	727^{+186}_{-123}	561	558	535	507	480	453	442
Hivel12	$12.5^{+1.8}_{-1.0}$	726^{+230}_{-138}	578	573	553	524	495	471	457
Hivel13	$6.4^{+0.3}_{-0.1}$	718^{+121}_{-87}	636	616	612	580	548	533	506
Hivel14	$11.6^{+2.0}_{-1.2}$	713^{+160}_{-108}	588	575	563	537	506	478	462
Hivel15	$8.1^{+0.3}_{-0.1}$	705^{+191}_{-121}	619	603	594	566	534	511	489
Hivel16	$9.0^{+0.5}_{-0.3}$	698^{+132}_{-104}	607	596	583	552	521	502	482
Hivel17	$6.6^{+0.2}_{-0.1}$	697^{+165}_{-137}	637	617	612	583	550	531	504
Hivel18	$9.3^{+1.1}_{-0.6}$	697^{+170}_{-110}	606	592	581	552	520	499	479
Hivel19	$9.3^{+0.6}_{-0.3}$	696^{+198}_{-131}	606	594	581	552	521	499	479
Hivel20	$10.5^{+0.6}_{-0.4}$	691^{+149}_{-118}	596	586	571	542	512	488	471

Notes. The 62nd to 68th columns of Table A4 are listed here for the 20 fastest HiVelSCs, which mainly includes the escape velocities estimated by the seven Galactic potential models (Paczynski 1990; Gnedin et al. 2005; Xue et al. 2008; Koposov et al. 2010; Kenyon et al. 2014; Bovy 2015; Watkins et al. 2019). The median value, lower uncertainty, and upper uncertainty of Galactocentric distance ($r_{\rm GC}$) are shown in the same column (the second column) in this table but separated into three columns, respectively, in Table A4 (from the 35th to 37th columns). The median value, lower uncertainty, and upper uncertainty of Galactocentric total velocity ($V_{\rm GC}$) are shown in the same column (the third column) in this table but separated into three columns, respectively, in Table A4 (from the 47th to 49th columns).

[a] Galactocentric distance and total velocity.

[b] Escape velocities in the seven Galactic potential models.

Table A2
Unbound Probabilities of the 20 Fastest HiVelSCs in the Seven Potential Models

ID	P_{gc}[a]	P_{MW}[b]	P_{ub}(W)[c]	P_{ub}(G)[c]	P_{ub}(Ke)[c]	P_{ub}(Ko)[c]	P_{ub}(P)[c]	P_{ub}(M)[c]	P_{ub}(X)[c]	Origin_Class[d]
Hivel1	0.000	1.000	0.996	0.998	1.000	1.000	1.000	1.000	1.000	HRS
Hivel2	0.000	0.993	0.995	0.999	1.000	1.000	1.000	1.000	1.000	HRS
Hivel3	0.000	1.000	1.000	1.000	1.000	1.000	1.000	1.000	1.000	HRS
Hivel4	0.000	0.039	0.969	0.973	0.978	0.991	0.996	0.999	0.999	OUT
Hivel5	0.000	0.000	0.975	0.981	0.984	0.990	0.997	0.999	1.000	OUT
Hivel6	0.000	0.002	0.861	0.898	0.904	0.951	0.981	0.989	0.997	OUT
Hivel7	0.000	0.994	0.928	0.947	0.953	0.981	0.995	0.998	1.000	HRS
Hivel8	0.000	0.000	0.992	0.997	0.999	1.000	1.000	1.000	1.000	OUT
Hivel9	0.000	0.852	0.804	0.831	0.852	0.912	0.935	0.951	0.969	HRS
Hivel10	0.001	0.003	0.837	0.874	0.894	0.939	0.972	0.989	0.999	OUT
Hivel11	0.000	0.848	0.900	0.913	0.940	0.961	0.983	0.994	0.996	HRS
Hivel12	0.000	0.415	0.843	0.854	0.886	0.929	0.965	0.980	0.988	OUT
Hivel13	0.000	0.000	0.821	0.868	0.876	0.942	0.979	0.987	0.997	OUT
Hivel14	0.000	0.997	0.863	0.885	0.910	0.942	0.982	0.994	0.996	HRS
Hivel15	0.000	0.995	0.759	0.790	0.809	0.871	0.931	0.959	0.978	HRS
Hivel16	0.000	0.009	0.800	0.830	0.855	0.923	0.965	0.984	0.993	OUT
Hivel17	0.000	1.000	0.659	0.713	0.732	0.797	0.864	0.915	0.953	HRS
Hivel18	0.000	1.000	0.782	0.816	0.839	0.908	0.961	0.979	0.990	HRS
Hivel19	0.000	0.022	0.736	0.775	0.798	0.857	0.909	0.938	0.962	OUT
Hivel20	0.000	0.999	0.779	0.809	0.837	0.904	0.946	0.975	0.983	HRS

Notes. The 69th to 78th columns of Table A4 are listed here for the 20 fastest HiVelSCs, which include the unbound probabilities in the seven potential models (Paczynski 1990; Gnedin et al. 2005; Xue et al. 2008; Koposov et al. 2010; Kenyon et al. 2014; Bovy 2015; Watkins et al. 2019), and the classification results of their origin.
[a] The probability that a star is derived from the GC.
[b] The probability that a star origins from the Galactic disk.
[c] The unbound probabilities in the seven Galactic potential models.
[d] The Origin classification including "HVS", "HRS", "RS", and "OUT".

Table A3
Atmospheric Parameters for the 20 Fastest HiVelSCs

ID	T_{eff}_LASP[a] (K)	log g_LASP[a] (dex)	[Fe/H]_LASP[a] (dex)	T_{eff}_DD-Payne[b] (K)	log g_DD-Payne[b] (dex)	[Fe/H]_DD-Payne[b] (dex)	[α/Fe]_DD-Payne[b] (dex)
Hivel1	4803 ± 19	1.89 ± 0.03	−1.40 ± 0.02	4919 ± 38	37.62 ± 2.22	−1.25 ± 0.06	0.28 ± 0.02
Hivel2	5384 ± 84	2.82 ± 0.14	−1.54 ± 0.08	5813 ± 47	46.96 ± 3.66	−1.24 ± 0.07	0.24 ± 0.04
Hivel3	4615 ± 228	4.86 ± 0.36	−1.48 ± 0.21	4801 ± 51	50.95 ± 4.93	−1.09 ± 0.09	0.17 ± 0.04
Hivel4	6553 ± 12	4.10 ± 0.02	−2.30 ± 0.02	7190 ± 49	48.50 ± 4.02	−1.87 ± 0.10	0.16 ± 0.03
Hivel5	4835 ± 121	1.54 ± 0.19	−2.20 ± 0.11	5366 ± 81	80.92 ± 2.37	−1.84 ± 0.13	0.22 ± 0.10
Hivel6	5415 ± 32	2.78 ± 0.05	−1.10 ± 0.03	5443 ± 29	29.04 ± 2.53	−1.12 ± 0.05	0.28 ± 0.02
Hivel7	6238 ± 214	3.97 ± 0.34	−1.60 ± 0.20	6175 ± 90	89.67 ± 3.35	−1.88 ± 0.18	0.30 ± 0.07
Hivel8	5401 ± 29	4.16 ± 0.05	−0.46 ± 0.03	5362 ± 24	24.47 ± 4.08	−0.41 ± 0.04	0.09 ± 0.01
Hivel9	4243 ± 42	0.75 ± 0.07	−1.29 ± 0.04	4290 ± 21	21.40 ± 1.17	−1.22 ± 0.04	0.10 ± 0.02
Hivel10	6151 ± 260	4.06 ± 0.41	−0.79 ± 0.24	⋯	⋯	⋯	−0.29 ± 0.02
Hivel11	4650 ± 48	1.53 ± 0.08	−1.43 ± 0.05	4798 ± 50	49.53 ± 1.92	−1.25 ± 0.07	0.27 ± 0.03
Hivel12	4928 ± 26	2.13 ± 0.04	−1.34 ± 0.02	5058 ± 35	34.58 ± 2.36	−1.20 ± 0.05	0.26 ± 0.02
Hivel13	5010 ± 59	2.31 ± 0.10	−1.38 ± 0.06	5054 ± 57	57.30 ± 2.32	−1.28 ± 0.08	0.26 ± 0.03
Hivel14	5013 ± 39	2.26 ± 0.06	−1.97 ± 0.04	5111 ± 40	40.42 ± 3.06	−1.94 ± 0.06	0.01 ± 0.02
Hivel15	6159 ± 108	4.17 ± 0.18	−0.97 ± 0.10	6118 ± 36	36.28 ± 4.14	−1.07 ± 0.07	0.18 ± 0.04
Hivel16	6336 ± 29	4.14 ± 0.05	−1.21 ± 0.03	6151 ± 27	27.28 ± 3.18	−1.31 ± 0.05	0.16 ± 0.02
Hivel17	6181 ± 129	4.05 ± 0.21	−1.51 ± 0.12	6220 ± 55	54.78 ± 3.95	−1.55 ± 0.10	0.18 ± 0.06
Hivel18	4660 ± 50	1.40 ± 0.08	−2.04 ± 0.05	5009 ± 47	46.74 ± 2.19	−1.70 ± 0.06	0.24 ± 0.03
Hivel19	4930 ± 49	2.36 ± 0.08	−1.22 ± 0.05	5024 ± 50	49.61 ± 2.52	−1.16 ± 0.07	0.25 ± 0.03
Hivel20	5271 ± 95	2.76 ± 0.16	−2.21 ± 0.09	5435 ± 54	53.93 ± 3.08	−2.00 ± 0.10	0.27 ± 0.06

Notes. The 79th to 92nd columns of Table A4 are listed here for the 20 fastest HiVelSCs, which are atmospheric parameters and α abundance estimated by the LASP and the data-driven Payne (DD-Payne) method, respectively. The measurements and uncertainties are shown in the same column in this table but separated into two columns in Table A4.
[a] Atmospheric parameters estimated by the LASP.
[b] Atmospheric parameters calculated by the DD-Payne method in Xiang et al. (2019).

Table A4
Description of Our HiVelSCs Catalog

Column	Name	Units	Description
1	ID	–	High-velocity star identifier[3]
2	specid	–	LAMOST DR7 identifier[1]
3	Gaia_designation	–	Gaia DR2 identifier[2]
4	R.A.	deg	Right ascension[2]
5	e_R.A.	deg	Right ascension error[2]
6	decl.	deg	Declination[2]
7	e_decl.	deg	Declination error[2]
8	S/N_r	–	r-band spectral signal-to-noise ratio[1]
9	Class	–	Spectral type[1]
10	RV_LASP	km s^{-1}	Radial velocity measured by the LASP[1]
11	e_RV_LASP	km s^{-1}	Radial velocity error given by the LASP[1]
12	pmra	mas yr^{-1}	Proper motion in right ascension[2]
13	e_pmra	mas yr^{-1}	Standard uncertainty in pmra[2]
14	pmdec	mas yr^{-1}	Proper motion in declination[2]
15	e_pmdec	mas yr^{-1}	Standard uncertainty in pmdec[2]
16	parallax	mas	Parallax[2]
17	e_parallax	mas	Standard uncertainty in parallax[2]
18	G	mag	G band mean magnitude[2]
19	G_BP	mag	$G_{\rm BP}$ band mean magnitude[2]
20	G_RP	mag	$G_{\rm RP}$ band mean magnitude[2]
21	astrometric_flag	–	A flag to mark whether a star has reliable astrometric parameters[3]
22	RV_LASP_Calibrate	km s^{-1}	LASP radial velocity corrected the zero-point[1]
23	r	kpc	Heliocentric distance[3]
24	el_r	kpc	Lower uncertainty on r[3]
25	eu_r	kpc	Upper uncertainty on r[3]
26	x	kpc	Cartesian Galactocentric x-coordinate[3]
27	el_x	kpc	Lower uncertainty on x[3]
28	eu_x	kpc	Upper uncertainty on x[3]
29	y	kpc	Cartesian Galactocentric y-coordinate[3]
30	el_y	kpc	Lower uncertainty on y[3]
31	eu_y	kpc	Upper uncertainty on y[3]
32	z	kpc	Cartesian Galactocentric z-coordinate[3]
33	el_z	kpc	Lower uncertainty on z[3]
34	eu_z	kpc	Upper uncertainty on z[3]
35	r_GC	kpc	Galactocentric distance[3]
36	el_r_GC	kpc	Lower uncertainty on $r_{\rm GC}$[3]
37	eu_r_GC	kpc	Upper uncertainty on $r_{\rm GC}$[3]
38	Vx	km s^{-1}	Cartesian Galactocentric x-velocity[3]
39	el_Vx	km s^{-1}	Lower uncertainty on V_x[3]
40	eu_Vx	km s^{-1}	Upper uncertainty on V_x[3]
41	Vy	km s^{-1}	Cartesian Galactocentric y-velocity[3]
42	el_Vy	km s^{-1}	Lower uncertainty on V_y[3]
43	eu_Vy	km s^{-1}	Upper uncertainty on V_y[3]
44	Vz	km s^{-1}	Cartesian Galactocentric z-velocity[3]
45	el_Vz	km s^{-1}	Lower uncertainty on V_z[3]
46	eu_Vz	km s^{-1}	Upper uncertainty on V_z[3]
47	V_GC	km s^{-1}	Cartesian Galactocentric total velocity[3]
48	el_V_GC	km s^{-1}	Lower uncertainty on $V_{\rm GC}$[3]
49	eu_V_GC	km s^{-1}	Upper uncertainty on $V_{\rm GC}$[3]
50	e	–	Orbit eccentricity[3]
51	el_e	–	Lower uncertainty on e[3]
52	eu_e	–	Upper uncertainty on e[3]
53	Zmax	kpc	Orbit maximum height above the Galactic disk[3]
54	el_Zmax	kpc	Lower uncertainty on $Z_{\rm max}$[3]
55	eu_Zmax	kpc	Upper uncertainty on $Z_{\rm max}$[3]
56	r_min	kpc	Minimum crossing radius[3]
57	el_r_min	kpc	Lower uncertainty on $r_{\rm min}$[3]
58	eu_r_min	kpc	Upper uncertainty on $r_{\rm min}$[3]
59	E_Phi_Infinity	kpc^2 Myr^{-2}	The difference between orbit energy E and potential energy at infinity[3]
60	el_E_Phi_Infinity	kpc^2 Myr^{-2}	Lower uncertainty on E_Phi_Infinity[3]
61	eu_E_Phi_Infinity	kpc^2 Myr^{-2}	Upper uncertainty on E_Phi_Infinity[3]
62	Vesc(W)	km s^{-1}	Escape velocity estimated by the potential model in Watkins et al. (2019)[3]
63	Vesc(G)	km s^{-1}	Escape velocity estimated by the potential model in Gnedin et al. (2005)[3]

Table A4
(Continued)

Column	Name	Units	Description
64	Vesc(Ke)	km s^{-1}	Escape velocity estimated by the potential model in Kenyon et al. (2014)[3]
65	Vesc(Ko)	km s^{-1}	Escape velocity estimated by the potential model in Koposov et al. (2010)[3]
66	Vesc(P)	km s^{-1}	Escape velocity estimated by the potential model in Paczynski (1990)[3]
67	Vesc(M)	km s^{-1}	Escape velocity estimated by the potential model in Bovy (2015)[3]
68	Vesc(X)	km s^{-1}	Escape velocity estimated by the potential model in Xue et al. (2008)[3]
69	Pgc	–	Probability of ejecting from the GC[3]
70	P_{MW}	–	Probability of ejecting from the Galactic disk[3]
71	Pub(W)	–	Unbound probability in the potential model in Watkins et al. (2019)[3]
72	Pub(G)	–	Unbound probability in the potential model in Gnedin et al. (2005)[3]
73	Pub(Ke)	–	Unbound probability in the potential model in Kenyon et al. (2014)[3]
74	Pub(Ko)	–	Unbound probability in the potential model in Koposov et al. (2010)[3]
75	Pub(P)	–	Unbound probability in the potential model in Paczynski (1990)[3]
76	Pub(M)	–	Unbound probability in the potential model in Bovy (2015)[3]
77	Pub(X)	–	Unbound probability under the potential model in Xue et al. (2008)[3]
78	Origin_Class	–	Origin classification including "HVS," "HRS," "RS" and "OUT"[3]
79	Teff_LASP	K	Effective temperature estimated by the LASP[3]
80	e_Teff_LASP	K	Uncertainty on T_{eff}_LASP[3]
81	log g_LASP	dex	Surface gravity estimated by the LASP[3]
82	e_log g_LASP	dex	Uncertainty on log(g)_LASP[3]
83	[Fe/H]_LASP	dex	Metallicity estimated by the LASP[3]
84	e_[Fe/H]_LASP	dex	Uncertainty on [Fe/H]_LASP[3]
85	Teff_DD-Payne	K	Effective temperature estimated by the data-driven Payne method[3]
86	e_Teff_DD-Payne	K	Uncertainty on T_{eff}_DD-Payne[3]
87	log g_DD-Payne	dex	Surface gravity estimated by the data-driven Payne method[3]
88	e_log g_DD-Payne	dex	Uncertainty on log(g)_DD-Payne[3]
89	[Fe/H]_DD-Payne	dex	Metallicity estimated by the data-driven Payne method[3]
90	e_[Fe/H]_DD-Payne	dex	Uncertainty on [Fe/H]_DD-Payne[3]
91	Alpha_Fe_DD-Payne	dex	α abudance estimated by the data-driven Payne method[3]
92	e_Alpha_Fe_DD-Payne	dex	Uncertainty on Alpha_Fe_DD-Payne[3]
93	conservative_result	–	HiVelSCs satisfy all more conservative criteria in Section 5.2[3]

Note. Parameters measured by this work such as distances and velocities correspond to the median of the distribution, and lower and upper uncertainties are derived from the 16th and 84th percentiles of the distribution, respectively. Entries labeled 1 are from the LAMOST catalog, entries labeled 2 are taken from the Gaia DR2 catalog (Gaia Collaboration et al. 2018a), and entries labeled 3 are derived in this paper. The complete catalog is available in the China-VO PaperData Repository. (1) For unbound HiVelSCs and bound HiVelSCs with $Z_{max} > 200$ kpc, we do not provide eccentricity e and the maximum height above the Galactic disk Z_{max}. (2) "–" represents null.

ORCID iDs

Yin-Bi Li (李荫碧) https://orcid.org/0000-0001-7607-2666
A-Li Luo (罗阿理) https://orcid.org/0000-0001-7865-2648
You-Jun Lu (陆由俊) https://orcid.org/0000-0002-1310-4664
Jiao Li (李蛟) https://orcid.org/0000-0002-2577-1990
Rui Wang (王瑞) https://orcid.org/0000-0001-6767-2395
Maosheng Xiang (向茂盛) https://orcid.org/0000-0002-5818-8769
Yuan-Sen Ting (丁源森) https://orcid.org/0000-0001-5082-9536
Tommaso Marchetti https://orcid.org/0000-0003-0064-0692
Shuo Li (李硕) https://orcid.org/0000-0002-8913-3605
Shuo Zhang (张硕) https://orcid.org/0000-0003-1454-1636
Kohei Hattori https://orcid.org/0000-0001-6924-8862
Hua-Wei Zhang (张华伟) https://orcid.org/0000-0002-7727-1699
Gang Zhao (赵刚) https://orcid.org/0000-0002-8980-945X

References

Abadi, M. G., Navarro, J. F., & Steinmetz, M. 2009, ApJL, 691, L63
Allende Prieto, C., Fernández-Alvar, E., Schlesinger, K. J., et al. 2014, A&A, 568, A7
An, D., Beers, T. C., Johnson, J. A., et al. 2013, ApJ, 763, 65
Andrae, R., Fouesneau, M., Creevey, O., et al. 2018, A&A, 616, A8
Arenou, F., Luri, X., Babusiaux, C., et al. 2018, A&A, 616, A17
Bailer-Jones, C. A. L. 2015, PASP, 127, 994
Bensby, T., Feltzing, S., & Lundström, I. 2003, A&A, 410, 527
Blaauw, A. 1961, BAN, 15, 265
Bland-Hawthorn, J., & Gerhard, O. 2016, ARA&A, 54, 529
Boeche, C., Chiappini, C., Minchev, I., et al. 2013, A&A, 553, A19
Bonaca, A., Conroy, C., Wetzel, A., et al. 2017, ApJ, 845, 101
Boubert, D., Erkal, D., Evans, N. W., & Izzard, R. G. 2017, MNRAS, 469, 2151
Boubert, D., & Evans, N. W. 2016, ApJL, 825, L6
Boubert, D., Guillochon, J., Hawkins, K., et al. 2018, MNRAS, 479, 2789
Boubert, D., Strader, J., Aguado, D., et al. 2019, MNRAS, 486, 2618
Bovy, J. 2015, ApJS, 216, 29
Bromley, B. C., Kenyon, S. J., Brown, W. R., et al. 2009, ApJ, 706, 925
Bromley, B. C., Kenyon, S. J., Brown, W. R., et al. 2018, ApJ, 868, 25
Bromley, B. C., Kenyon, S. J., Geller, M. J., et al. 2006, ApJ, 653, 1194
Brown, W. R. 2015, ARA&A, 53, 15
Brown, W. R., Geller, M. J., & Kenyon, S. J. 2009, ApJ, 690, 1639
Brown, W. R., Geller, M. J., & Kenyon, S. J. 2012, ApJ, 751, 55
Brown, W. R., Geller, M. J., & Kenyon, S. J. 2014, ApJ, 787, 89
Brown, W. R., Geller, M. J., Kenyon, S. J., & Kurtz, M. J. 2005, ApJL, 622, L33
Brown, W. R., Geller, M. J., Kenyon, S. J., & Kurtz, M. J. 2006, ApJ, 647, 303
Brown, W. R., Lattanzi, M. G., Kenyon, S. J., et al. 2018, ApJ, 866, 39
Caffau, E., Monaco, L., Bonifacio, P., et al. 2020, A&A, 638, A122
Capuzzo-Dolcetta, R., & Fragione, G. 2015, MNRAS, 454, 2677
Carollo, D., Beers, T. C., Chiba, M., et al. 2010, ApJ, 712, 692
Carollo, D., Beers, T. C., Lee, Y. S., et al. 2007, Natur, 450, 1020
Cicone, C., Maiolino, R., & Marconi, A. 2016, A&A, 588, A41
Conroy, C., Naidu, R. P., Zaritsky, D., et al. 2019, ApJ, 887, 237

Cui, X.-Q., Zhao, Y.-H., Chu, Y.-Q., et al. 2012, RAA, 12, 1197
Das, P., & Binney, J. 2016, MNRAS, 460, 1725
de la Fuente Marcos, R., & de la Fuente Marcos, C. 2019, A&A, 627, A104
Du, C., Li, H., Liu, S., et al. 2018a, ApJ, 863, 87
Du, C., Li, H., Newberg, H. J., et al. 2018b, ApJL, 869, L31
Du, C., Li, H., Yan, Y., et al. 2019, ApJS, 244, 4
Edelmann, H., Napiwotzki, R., Heber, U., Christlieb, N., & Reimers, D. 2005, ApJL, 634, L181
Erkal, D., Boubert, D., Gualandris, A., et al. 2019, MNRAS, 483, 2007
Favia, A., West, A. A., & Theissen, C. A. 2015, ApJ, 813, 26
Fragione, G., & Capuzzo-Dolcetta, R. 2016, MNRAS, 458, 2596
Fragione, G., Ginsburg, I., & Kocsis, B. 2018, ApJ, 856, 92
Fragione, G., & Gualandris, A. 2018, MNRAS, 475, 4986
Gaia Collaboration, Brown, A. G. A., Vallenari, A., et al. 2018a, A&A, 616, A1
Gaia Collaboration, Mignard, F., Klioner, S. A., et al. 2018b, A&A, 616, A14
Gaia Collaboration, Prusti, T., de Bruijne, J. H. J., et al. 2016, A&A, 595, A1
Geier, S., Fürst, F., Ziegerer, E., et al. 2015, Sci, 347, 1126
Gnedin, O. Y., Gould, A., Miralda-Escudé, J., & Zentner, A. R. 2005, ApJ, 634, 344
Gvaramadze, V. V., Gualandris, A., & Portegies Zwart, S. 2009, MNRAS, 396, 570
Hattori, K., Valluri, M., Bell, E. F., et al. 2018, ApJ, 866, 121
Hawkins, K., Kordopatis, G., Gilmore, G., et al. 2015, MNRAS, 447, 2046
Heber, U., Edelmann, H., Napiwotzki, R., Altmann, M., & Scholz, R.-D. 2008, A&A, 483, L21
Hills, J. G. 1988, Natur, 331, 687
Hirsch, H. A., Heber, U., O'Toole, S. J., & Bresolin, F. 2005, A&A, 444, L61
Huang, Y., Liu, X.-W., Chen, B.-Q., et al. 2018, AJ, 156, 90
Huang, Y., Liu, X.-W., Zhang, H.-W., et al. 2017, ApJL, 847, L9
Irrgang, A., Geier, S., Heber, U., et al. 2019, A&A, 628, L5
Irrgang, A., Kreuzer, S., Heber, U., et al. 2018a, A&A, 615, L5
Irrgang, A., Kreuzer, S., & Heber, U. 2018b, A&A, 620, A48
Johnson, D. R. H., & Soderblom, D. R. 1987, AJ, 93, 864
Kenyon, S. J., Bromley, B. C., Brown, W. R., & Geller, M. J. 2014, ApJ, 793, 122
Kenyon, S. J., Bromley, B. C., Geller, M. J., et al. 2008, ApJ, 680, 312
Kollmeier, J. A., Gould, A., Knapp, G., & Beers, T. C. 2009, ApJ, 697, 1543
Koposov, S. E., Boubert, D., Li, T. S., et al. 2020, MNRAS, 491, 2465
Koposov, S. E., Rix, H.-W., & Hogg, D. W. 2010, ApJ, 712, 260
Kordopatis, G., Gilmore, G., Wyse, R. F. G., et al. 2013a, MNRAS, 436, 3231
Kordopatis, G., Hill, V., Irwin, M., et al. 2013b, A&A, 555, A12
Kreuzer, S., Irrgang, A., & Heber, U. 2020, A&A, 637, A53
Li, J., Jia, S., Gao, Y., et al. 2020, RAA, 20, 042
Li, Y., Luo, A., Zhao, G., et al. 2012, ApJL, 744, L24
Li, Y.-B., Luo, A.-L., Zhao, G., et al. 2015, RAA, 15, 1364
Li, Y.-B., Luo, A.-L., Zhao, G., et al. 2018, AJ, 156, 87
Lindegren, L., Hernández, J., Bombrun, A., et al. 2018, A&A, 616, A2
Liu, C., Fu, J., Shi, J., et al. 2020, arXiv:2005.07210v1
Liu, S., Du, C., Newberg, H. J., et al. 2018, ApJ, 862, 163
Luo, A.-L., Zhang, H.-T., Zhao, Y.-H., et al. 2012, RAA, 12, 1243
Luo, A.-L., Zhao, Y.-H., Zhao, G., et al. 2015, RAA, 15, 1095
Mackereth, J. T., Schiavon, R. P., Pfeffer, J., et al. 2019, MNRAS, 482, 3426
Marchetti, T., Rossi, E. M., & Brown, A. G. A. 2019, MNRAS, 490, 157
Nissen, P. E., & Schuster, W. J. 2010, A&A, 511, L10
O'Leary, R. M., & Loeb, A. 2008, MNRAS, 383, 86
Paczynski, B. 1990, ApJ, 348, 485
Perets, H. B., & Šubr, L. 2012, ApJ, 751, 133
Raddi, R., Hollands, M. A., Koester, D., et al. 2019, MNRAS, 489, 1489
Ryan, S. G., & Smith, I. M. 2003, MNRAS, 341, 199
Schönrich, R. 2012, MNRAS, 427, 274
Schönrich, R., Asplund, M., & Casagrande, L. 2011, MNRAS, 415, 3807
Schönrich, R., Binney, J., & Dehnen, W. 2010, MNRAS, 403, 1829
Schuster, W. J., Moitinho, A., Márquez, A., et al. 2006, A&A, 445, 939
Schuster, W. J., & Nissen, P. E. 1988, A&AS, 73, 225
Sesana, A., Haardt, F., & Madau, P. 2006, ApJ, 651, 392
Sesana, A., Haardt, F., & Madau, P. 2007, MNRAS, 379, L45
Shen, K. J., Boubert, D., Gänsicke, B. T., et al. 2018, ApJ, 865, 15
Sherwin, B. D., Loeb, A., & O'Leary, R. M. 2008, MNRAS, 386, 1179
Su, D.-Q., & Cui, X.-Q. 2004, ChJAA, 4, 1
Teyssier, M., Johnston, K. V., & Shara, M. M. 2009, ApJL, 707, L22
Tillich, A., Geier, S., Heber, U., et al. 2009, JPhCS, 172, 012009
Ting, Y.-S., Rix, H.-W., Conroy, C., et al. 2017, ApJL, 849, L9
Vennes, S., Nemeth, P., Kawka, A., et al. 2017, Sci, 357, 680
Wang, B., & Han, Z. 2009, A&A, 508, L27
Wang, B., Justham, S., & Han, Z. 2013, A&A, 559, A94
Wang, S.-G., Su, D.-Q., Chu, Y.-Q., Cui, X., & Wang, Y.-N. 1996, ApOpt, 35, 5155
Watkins, L. L., van der Marel, R. P., Sohn, S. T., et al. 2019, ApJ, 873, 118
Xiang, M., Ting, Y.-S., Rix, H.-W., et al. 2019, ApJS, 245, 34
Xiang, M. S., Liu, X. W., Yuan, H. B., et al. 2015, MNRAS, 448, 822
Xu, Y., Newberg, H. J., Carlin, J. L., et al. 2015, ApJ, 801, 105
Xue, X.-X., Rix, H.-W., Ma, Z., et al. 2015, ApJ, 809, 144
Xue, X. X., Rix, H. W., Zhao, G., et al. 2008, ApJ, 684, 1143
Youakim, K., Starkenburg, E., Martin, N. F., et al. 2020, MNRAS, 492, 4986
Yu, Q., & Madau, P. 2007, MNRAS, 379, 1293
Yu, Q., & Tremaine, S. 2003, ApJ, 599, 1129
Yuan, H.-B., Liu, X.-W., Huo, Z.-Y., et al. 2015, MNRAS, 448, 855
Zhang, F., Lu, Y., & Yu, Q. 2010, ApJ, 722, 1744
Zhao, G., Chen, Y.-Q., Shi, J.-R., et al. 2006, ChJAA, 6, 265
Zhao, G., Zhao, Y.-H., Chu, Y.-Q., Jing, Y.-P., & Deng, L.-C. 2012, RAA, 12, 723
Zheng, Z., Carlin, J. L., Beers, T. C., et al. 2014, ApJL, 785, L23
Zhong, J., Chen, L., Liu, C., et al. 2014, ApJL, 789, L2
Zuo, W., Du, C., Jing, Y., et al. 2017, ApJ, 841, 59